



## Winter to summer oceanographic observations in the Arctic Ocean north of Svalbard

Amelie Meyer, Arild Sundfjord, Ilker Fer, Christine Provost, Nicolas Villaceros Robineau, Zoé Koenig, Ingrid H. Onarheim, Lars H. Smedsrud, Pedro Duarte, Paul A. Dodd, et al.

### ► To cite this version:

Amelie Meyer, Arild Sundfjord, Ilker Fer, Christine Provost, Nicolas Villaceros Robineau, et al.. Winter to summer oceanographic observations in the Arctic Ocean north of Svalbard. Journal of Geophysical Research. Oceans, 2017, 122 (8), pp.6218-6237. 10.1002/2016JC012391 . hal-01492014

**HAL Id: hal-01492014**

**<https://hal.science/hal-01492014>**

Submitted on 4 Jan 2022

**HAL** is a multi-disciplinary open access archive for the deposit and dissemination of scientific research documents, whether they are published or not. The documents may come from teaching and research institutions in France or abroad, or from public or private research centers.

L'archive ouverte pluridisciplinaire **HAL**, est destinée au dépôt et à la diffusion de documents scientifiques de niveau recherche, publiés ou non, émanant des établissements d'enseignement et de recherche français ou étrangers, des laboratoires publics ou privés.



Distributed under a Creative Commons Attribution - NonCommercial - NoDerivatives 4.0 International License



## RESEARCH ARTICLE

10.1002/2016JC012391

## Special Section:

Atmosphere-ice-ocean-ecosystem Processes in a Thinner Arctic Sea Ice Regime: the Norwegian Young Sea Ice Cruise 2015 (N-ICE2015)

## Key Points:

- N-ICE2015 Arctic winter oceanographic observations are a key contribution in a region with extremely sparse winter data coverage
- Yermak Branch of Atlantic Water inflow is observed retroflecting around the northern tip of the Yermak Plateau
- Late spring shallow mixed layer over the Yermak Plateau associated with large sea ice melt

## Correspondence to:

A. Meyer,  
Amelie.Meyer@npolar.no

## Citation:

Meyer, A., et al. (2017), Winter to summer oceanographic observations in the Arctic Ocean north of Svalbard, *J. Geophys. Res. Oceans*, 122, 6218–6237, doi:10.1002/2016JC012391.

Received 28 SEP 2016

Accepted 23 JAN 2017

Accepted article online 31 JAN 2017

Published online 4 AUG 2017

Corrected 8 SEP 2017

This article was corrected on 8 SEP 2017. See the end of the full text for details.

© 2017. The Authors.

This is an open access article under the terms of the Creative Commons Attribution-NonCommercial-NoDerivs License, which permits use and distribution in any medium, provided the original work is properly cited, the use is non-commercial and no modifications or adaptations are made.

# Winter to summer oceanographic observations in the Arctic Ocean north of Svalbard

Amelie Meyer<sup>1</sup> , Arild Sundfjord<sup>1</sup> , Ilker Fer<sup>3</sup> , Christine Provost<sup>2</sup> , Nicolas Villaciers Robineau<sup>2</sup>, Zoe Koenig<sup>2</sup> , Ingrid H. Onarheim<sup>3</sup> , Lars H. Smedsrud<sup>3</sup> , Pedro Duarte<sup>1</sup> , Paul A. Dodd<sup>1</sup> , Robert M. Graham<sup>1,4</sup> , Sunke Schmidt<sup>5</sup> , and Hanna M. Kauko<sup>1</sup>

<sup>1</sup>Norwegian Polar Institute, Fram Centre, Tromsø, Norway, <sup>2</sup>LOCEAN, Université Pierre et Marie Curie, Paris Cedex, France,

<sup>3</sup>Geophysical Institute, University of Bergen and Bjerknes Centre for Climate Research, Bergen, Norway, <sup>4</sup>Alfred Wegener Institute, Helmholtz Centre for Polar and Marine Research, Bremerhaven, Germany, <sup>5</sup>GEO-MAR, Helmholtz Centre for Ocean Research, Kiel, Germany

**Abstract** Oceanographic observations from the Eurasian Basin north of Svalbard collected between January and June 2015 from the N-ICE2015 drifting expedition are presented. The unique winter observations are a key contribution to existing climatologies of the Arctic Ocean, and show a ~100 m deep winter mixed layer likely due to high sea ice growth rates in local leads. Current observations for the upper ~200 m show mostly a barotropic flow, enhanced over the shallow Yermak Plateau. The two branches of inflowing Atlantic Water are partly captured, confirming that the outer Yermak Branch follows the perimeter of the plateau, and the inner Svalbard Branch the coast. Atlantic Water observed to be warmer and shallower than in the climatology, is found directly below the mixed layer down to 800 m depth, and is warmest along the slope, while its properties inside the basin are quite homogeneous. From late May onwards, the drift was continually close to the ice edge and a thinner surface mixed layer and shallower Atlantic Water coincided with significant sea ice melt being observed.

## 1. Introduction

The Arctic Ocean is connected to the Atlantic Ocean via the deep Fram Strait and the shallow Barents Sea. The exchange in the Fram Strait is dominated by northward flowing warm and saline Atlantic Water (AW) and southward cold Arctic water near the surface [Rudels et al., 2000; Spall, 2013; Rudels et al., 2015]. The warm AW is the primary source of heat for the Arctic Ocean [Aagaard and Greisman, 1975; Carmack et al., 2015].

In Fram Strait, the inflow of warm AW advected by the West Spitsbergen Current splits as it reaches the Yermak Plateau [Aagaard et al., 1987]. The Svalbard Branch follows the topography inshore of the Yermak Plateau between the 400 and 500 m isobaths [Sirevaag and Fer, 2009]. The Yermak Branch circulates anticyclonically around the Yermak Plateau's western slope and follows the 1500 m isobath [Perkin and Lewis, 1984; Muench et al., 1992; Gascard et al., 1995]. A substantial fraction of the Yermak Branch has been observed to cross the Plateau eastward at 80.4°N through the Yermak Pass at 700 m depth [Gascard et al., 1995], but this has not been confirmed by other studies, possibly due to the scarcity of observations in that area (Figure 1). Another part of the Yermak Branch detaches from the continental slope and recirculates across Fram Strait [Bourke et al., 1988]. It is thought that the remaining part of the Yermak Branch rejoins the inshore branch northeast of Svalbard but pathways past the northern tip of the Plateau are unclear. East of Svalbard, AW flows eastward along the slope of the Eurasian continent [Treshnikov, 1977], cooling and freshening, before it is eventually transported back to the Atlantic Ocean through the western Fram Strait [Lique et al., 2010; Polyakov et al., 2012] (Figure 1).

The Yermak Plateau is a local hotspot for vertical mixing and cooling of AW [Fer et al., 2015]. Strong tidal currents around the slopes of the Plateau lead to increased internal wave activity and therefore enhanced mixing rates [Padman and Dillon, 1991; Wijesekera et al., 1993; Fer et al., 2010]. Mixing causes water mass modification affecting regional ice cover [Fer et al., 2015]. North of Svalbard, inflowing AW

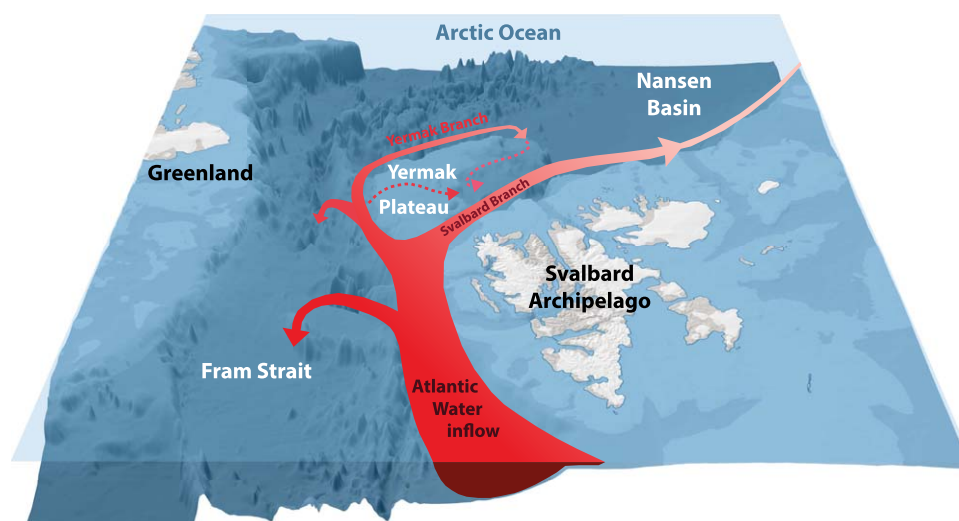


**Figure 1.** Regional circulation schematic of Atlantic Water inflow in Fram Strait and Nansen Basin, west and north of the Svalbard Archipelago following Sirevaag and Fer [2009] and Polyakov et al. [2012]. Dashed arrows represent uncertain Atlantic Water pathways around the Yermak Plateau and across the Plateau through the Yermak Pass. Bathymetry is from the ETOPO1 data set [Amante and Eakins, 2009].

interacts with the Arctic sea ice, and a fresher upper layer of Polar Water, is created [Onarheim et al., 2014; Rudels et al., 2015]. This region is therefore key for understanding the formation of the cold halocline that insulates sea ice from warm AW [Rudels et al., 2004]. As noted by Steele and Boyd [1998], processes that create the Arctic Ocean stratification are best identified using winter observations when these processes are taking place.

The AW inflow to the Arctic has been warming since the late 1970s with the strongest warming signal over the Svalbard slope [Grotefendt et al., 1998; Schauer et al., 2004; Ivanov et al., 2009; Polyakov et al., 2012; Beszczynska-Möller et al., 2012]. The warming of the AW layer could lead to substantial melt of the Arctic sea ice in particular near the AW source along the Svalbard continental slope [Polyakov et al., 2013; Onarheim et al., 2014; Carmack et al., 2015].

The Arctic Ocean is undersampled compared to much of the world ocean [Abrahamsen, 2014]. Estimating trends and understanding mechanisms in an extreme seasonal environment is a challenge with few comprehensive observational campaigns outside the spring and summer periods [Grotefendt et al., 1998].

The Norwegian young sea ICE expedition (N-ICE2015) took place north of Svalbard in 2015 to investigate the new thinner Arctic sea ice regime [Renner et al., 2013] and associated interactions between the ice, ocean, and atmosphere, and the feedbacks between physical and biogeochemical processes [Granskog et al., 2016]. We present hydrographic and ocean current observations collected from January to June 2015 during N-ICE2015 in the Nansen Basin and over the Yermak Plateau. These 6 months of observations, spanning the winter and spring is a unique data set and provides the oceanographic context for topical studies presented in N-ICE2015 companion papers. We investigate the hydrography and circulation, focusing on the AW pathways, characteristics, and impacts on sea ice. The data collection and quality control are described in section 2. In section 3, we give an overview of the water mass distribution, seasonal mixed layer, seasonal and regional variability, and currents. We discuss the implications in section 4 and conclude in section 5.

## 2. Data and Methods

### 2.1. N-ICE2015 Expedition

Between January and June 2015, during the N-ICE2015 expedition the R.V. Lance completed four drifts in the Arctic Ocean north of Svalbard, moored each time to a different sea ice floe (Figure 2 and Table 1). On each floe, hereinafter referred to as Floes 1–4, an ice camp was set up and oceanographic data as well as atmospheric, sea ice, snow, and biogeochemical data were collected [Granskog et al., 2016].

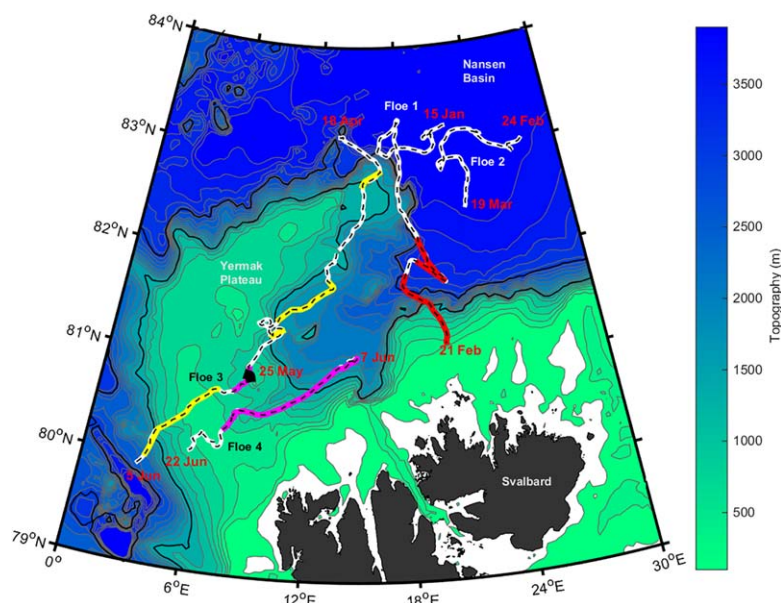


**Figure 2.** Trajectories of the four N-ICE2015 drift floes between 15 January and 22 June 2015 with underlying topographic contours ranging from 100 to 5000 m at 200 m intervals. Presence of Atlantic Water in the water column is indicated and labelled from either the Yermak Branch (yellow drift track), from undetermined origin (magenta drift track), or from the Svalbard Branch (red drift track). The 3000 and 1500 m isobaths represent the limits between the deep Nansen Basin, the slope areas and the shallower Yermak Plateau (thick black lines). Key dates are indicated in red.

The first drift took place in January and February 2015 lasting 38 days, partly in the Nansen Basin, partly at the northern edge of the Yermak Plateau, finishing on the Svalbard continental slope (Table 1). Drift 2 lasted 24 days over the Nansen Basin during February and March 2015. Drift 3, the longest, lasted 49 days from April until June 2015 from the northern slope of the Yermak Plateau, to the southern edge of the Plateau. Finally drift 4 took 16 days and covered a similar track to the last part of drift 3 on the Yermak Plateau. Drift 1 and 2 took place during winter, with drift 1 in full darkness and the first sunrise on 1 March 2015 during drift 2. Drift 3 and 4 took place during spring with the last sunset on 5 April 2015 during drift 3.

## 2.2. Collected Data

In this study, temperature and salinity profiles from several instruments are used: profiles from a vessel-mounted CTD processed to 1 m vertical average, profiles from Ice-Atmosphere-Arctic Ocean Observing System (IAOOS) profilers processed to 1 m vertical average, and profiles from microstructure profilers processed to 0.2 m vertical average). Also used in this study are dissolved oxygen concentrations from discrete

**Table 1.** N-ICE2015 Expedition Overview and Data Sets Used in This Study, Publicly Available at the Norwegian Polar Data Centre [Dodd et al., 2016; Meyer et al., 2016b, 2016; Provost et al., 2016; Dodd et al., 2016]

Ice Drift	Floe 1	Floe 2	Floe 3	Floe 4
Season	Winter	Winter	Spring	Spring
Start date	15 Jan 2015	24 Feb 2015	18 Apr 2015	7 Jun 2015
Start position	83.2°N 21.6°E	83°N 27.4°E	83.2°N 13.5°E	81.1°N 14.4°E
End date	21 Feb 2015	19 Mar 2015	5 Jun 2015	22 Jun 2015
End position	81.2°N 20.3°E	82.5°N 22.6°E	79.9°N 3.1°E	80.1°N 5.7°E
Duration (days)	38	24	49	16
Number of ship CTD casts	11	5	29	6
Number of on-ice CTD casts	21	19	39	13
Number of microstructure profiles (sets)	71 (21)	55 (25)	329 (94)	128 (29)
Number of IAOOS buoy profiles	112	16		
Vessel-mounted ADCP	15 Jan to 21 Feb 2015 38 days	24 Feb to 3 Mar 2015 8 days	18 Apr to 5 Jun 2015 49 days	7 Jun to 22 Jun 2015 16 days
Long Ranger ADCP			3 May to 4 Jun 2015 33 days	11 Jun to 19 Jun 2015 9 days

water samples, current velocity profiles from a medium range vessel-mounted ADCP (hourly temporal and 8 m vertical average), and current velocity profiles from a long ranger ADCP suspended beneath the ice floe (hourly temporal and 8 m vertical average). Each instrument and the associated data set are described in the following sections and summarized in Table 1. The data were analyzed using the Thermodynamic Equation of SeaWater 2010 (TEOS-10) and conservative temperature (CT) and Absolute Salinity (SA) is used throughout the text [McDougall *et al.*, 2012].

### 2.2.1. Ship-Board CTD Data

The ship-board CTD was a Sea-Bird Electronics SBE911 plus with two sets of sensors attached to a multibottle Sea-Bird carousel water sampler holding 11 Niskin bottles of 8 L each. Separate water samples for salinity analyses were drawn from the Niskin bottles immediately after the CTD package was secured in a heated area. These salinity samples were analyzed at sea using a Guildline Portasal salinometer with accuracy ca.  $\pm 0.003$ .

Prior to and after the N-ICE2015 expedition, the CTD sensors were calibrated at Sea-Bird. The temperature sensors drifts were negligible. The conductivity sensors had drifted and conductivity slope corrections were calculated using bottle salinity measurements. The data accuracy for conductivity estimates was  $\pm 0.0003 \text{ S m}^{-1}$  and for temperature of  $\pm 0.001^\circ\text{C}$ .

A total of 51 ship CTD casts were carried out of which 25 stopped just above the seafloor. The remainder were shallow casts (less than 200 m) to collect biological water samples. The ship CTD sampling was usually weekly, except when interrupted between the 16 February and the 20 March 2015. During this period, sea ice under and by the side of the ship stacked up to 8 m thick, making the CTD hole maintenance impossible.

### 2.2.2. IAOOS Profilers Data

Two IAOOS buoys (<http://iaaos.ipev.fr/index.php?lang=en>) [Provost *et al.*, 2015; Koenig *et al.*, 2016] that carried ice-tethered profilers manufactured by NKE (PROVOR SPI) were deployed during Floe 1. The profilers were equipped with a Seabird 41CP CTD and an Aanderaa 4330 optode for dissolved oxygen. The profilers were set to collect two profiles per day down to 500 m depth, and gathered a total of 112 profiles. In addition, during Floes 1 and 2, tests were carried out involving a profiler on a 800 m long instrumented line in a tent-covered testing-hole. A total of 42 profiles used in this study were obtained with this set up (26 during Floes 1 and 16 during Floe 2). The vertical resolution of the processed CTD data is 1 dbar in the upper 400 dbars, 5 dbars from 400 to 550 dbars and 10 dbars from 550 to 850 dbars. The vertical resolution in dissolved oxygen is 2 dbars over all depths.

The profiler salinity data were calibrated using the ship CTD salinity [Koenig *et al.*, 2016]. Following quality control, all the temperature profiles were retained and 1% of the salinity and dissolved oxygen profiles were removed. Resulting data accuracy was  $\pm 0.002^\circ\text{C}$  for temperature,  $\pm 0.02$  for salinity, and  $\pm 3 \mu\text{mol kg}^{-1}$  for dissolved oxygen.

### 2.2.3. Microstructure Profiler Data

A total of 588 microstructure profiles were collected in 173 sets with two loosely tethered free-fall MSS-90 microstructure profilers [Prandke and Stips, 1998] developed by ISW Wassermesstechnik. A set, which corresponds here to consecutively sampled profiles, was usually composed of three profiles during the N-ICE2015 expedition. The profilers had precision conductivity, temperature, and depth sensors as well as turbulence sensors including two airfoil shear probes, a fast response thermistor, and a microconductivity sensor. Here we use the CTD profiles while details of the microstructure data processing and a description of the vertical mixing and turbulence characteristics can be found in Meyer *et al.* [2017].

The microstructure profilers were deployed through a hole in the sea ice from a heated tent a few hundred meters away from the ship. The profiles (only the downcasts are used) started immediately below the ice and reached on average 150 m during Floe 1 and 300 m during Floes 2, 3, and 4. Data processing followed Fer [2006]. High-resolution profiles, sampled at 1024 Hz, were vertically averaged to 20 cm. The CTD data from the microstructure profilers were compared with the ship CTD data for validation, and salinity drift corrections of  $0.021 \text{ g kg}^{-1}$  for one and  $0.065 \text{ g kg}^{-1}$  for the second profiler were applied.

### 2.2.4. Dissolved Oxygen Data (Water Samples)

A total of 175 samples of dissolved oxygen were collected directly from Niskin bottles on either the ship CTD rosette (68 samples) or from bottles on a Hydro-Bios water sampler deployed from the sea ice (107 samples). This small water sampler (SlimLine 6) with integrated CT-set, hereinafter "on-ice CTD," was



operated from the same tent and hole as the microstructure profiler, several hundred meters away from R.V. Lance. Individual sampling bottles with a nominal capacity of 115 mL were used. The analysis and calculations followed the modified Winkler procedure described in *Carpenter* [1965]: sulfuric acid had 50% volume concentration and the concentration of thiosulfate stock solution was 0.18 M. Titrations were carried out in two 50 mL aliquots taken from the dissolved oxygen bottles to check the reproducibility of the results. Consecutive titrations led to nonsignificantly different results. A digital Solarus burette from Hirschmann was used. Standards and blank were determined every time measurements were made. Dissolved oxygen concentrations were calculated in  $\text{mL L}^{-1}$  and converted to  $\mu\text{mol kg}^{-1}$  using potential temperature and surface pressure [Weiss, 1970].

#### 2.2.5. Current Data: Vessel-Mounted ADCP Data

Current velocity in the upper 150 m was measured by a vessel-mounted broadband 150 kHz acoustic Doppler current profiler (ADCP) (Teledyne RD Instrument (RDI)). Vessel-mounted ADCP data were collected near continuously between 15 January and 22 June 2015, with a gap in data between 3 March and 19 March 2015 (Table 1) due to large ridging events blocking the ADCP transducers with sea ice. Profiles were averaged hourly in 8 m vertical bins with the first bin centered at 23 m.

#### 2.2.6. Current Data: Long Ranger ADCP Data

During part of the N-ICE2015 expedition, time series of velocity were collected using a downward-looking RDI 75 kHz Long Ranger ADCP (Table 1). This ADCP was deployed just under the sea ice suspended with a chain and secured to the ice floe several hundreds of meters away from the ship. During drift 3, the instrument averaged 40 velocity profiles (pings) at 10 min intervals in 8 m thick cells, with the first cell centered at 21 m, while during drift 4, 55 velocity profiles were averaged at 20 min intervals, with the first cell centered at 19 m. Ensembles with excessive tilt (pitch and roll more than  $\pm 20^\circ$ ), and bins with weak average echo intensity (less than 40 counts) or less than 50% good three-beam and four-beam solutions were discarded. Absolute current velocity was obtained by adding the ice velocity as measured by the ship's Global Positioning System (GPS) to the relative velocity profile. The final vertical range of the Long Ranger ADCP data was 480 m which is typical for Arctic waters where acoustic scatterer concentrations are low.

### 2.3. Tides

In order to estimate the relative contribution of tides and background flows in the observed velocities, two approaches were used. First, tidal predictions from a model were derived along the drift tracks. Second, we attempted to isolate the tidal signal from the velocity observations. Both estimates are compared and discussed in the section 3.

#### 2.3.1. Tidal Model: AOTIM-5 Tidal Current Predictions

We use the Arctic Ocean Tidal Inverse Model (AOTIM-5) [Padman and Erofeeva, 2004] to estimate the tidal current velocities associated with the four most energetic tidal components ( $M_2$ ,  $S_2$ ,  $O_1$ , and  $K_1$ ) along the N-ICE2015 drift trajectories. The model provides 5 km horizontal grid resolution barotropic tidal velocities based on the *Egbert et al.* [1994] data assimilation scheme using all available tide gauge data in the Arctic Ocean.

#### 2.3.2. Tidal Current Observations: Complex Demodulation

Our current observations were collected from a drifting platform. The time series are therefore affected by both temporal and spatial variability, and standard tidal harmonic analysis cannot be used. Using complex demodulation, we attempted to isolate the tidal signals in the ADCP current data time series. The algorithm is described in *Emery and Thomson* [2001, chap. 5, pp. 402–403]. Rotary component amplitude and phase of the diurnal and semidiurnal tides were estimated at, respectively, 24 and 12 h frequencies using 48 h long segments. Tidal estimates are not sensitive to the exact chosen time segment; the latest is determined by a compromise between too little data (short-time segment) and decreasing precision (large time segment). We cannot distinguish between the different constituents in the diurnal band or in the semidiurnal band. Furthermore, the inertial frequency is close to the semidiurnal band at these latitudes and will contaminate the tidal estimates (for the clockwise rotary component).

### 2.4. Climatologies and Reanalysis Products

#### 2.4.1. Ocean Climatology: MIMOC

The global monthly isopycnal mixed-layer ocean climatology (MIMOC) covers the 0–1950 dbar range with  $0.5^\circ \times 0.5^\circ$  spatial resolution, uses objective mapping routines and emphasizes data from the last decade

[Schmidt et al., 2013]. For each location of observations along the N-ICE2015 drift tracks, we linearly interpolate MIMOC in space and time to derive the best guess climatological values from MIMOC for comparison with our observations. Thus, each interpolated MIMOC profile is based on the eight MIMOC profiles closest in space and time.

#### 2.4.2. Reanalysis Product: ERA-Interim

The ERA-Interim reanalysis data set is a global atmospheric product that is updated in near real time. It is based on the ECMWF integrated Forecast System [Dee et al., 2011]. It uses a fixed version of a numerical weather prediction system to produce reanalysed data. The spatial resolution is approximately 80 km with 60 vertical levels, while the temporal resolution is 6 hourly.

### 3. Results

#### 3.1. Environmental Conditions

The drifts started inside the pack ice, and distance to open water decreased over time. The maximum distance to open water was at the start of Floe 2 with 474 km, and the minimum occurred at the end of Floe 4 with only 11 km. The overall mean distance to open water was 142 km. Distance to open water was estimated as the shortest distance from the R.V. Lance to the inner edge of the ice class “open water” (<10%) based on navigational sea ice charts produced by the Norwegian Meteorological Institute from satellite data [Itkin et al., 2017]. Floes 1 and 2 during winter started out well inside the Nansen Basin with bottom depths ~4000 m. As the different drifts approached open water and Fram Strait, bottom depth generally decreased to ~500–800 m above the Yermak Plateau.

Air temperatures below  $-40^{\circ}\text{C}$  occurred in January and February, while the lowest during March was approximately  $-20^{\circ}\text{C}$ . Air temperatures were usually  $-10^{\circ}\text{C}$  in May and approached  $0^{\circ}\text{C}$  in June [Cohen et al., 2017; Hudson et al., 2015]. Throughout the four drifts, a total of 18 atmospheric storms were recorded with roughly equal numbers in winter and spring [Cohen et al., 2017, Table 2]. Storms herein cover periods when 10 min averaged wind speed was continuously greater than  $8\text{ m s}^{-1}$  for at least 1 h. Major storms are those that are associated with a pressure decrease that exceeds 5 hPa in 6 h. The mean environmental conditions for each drift are given in Table 2. For a general description of the atmospheric conditions during the N-ICE2015 expedition [see Cohen et al., 2017].

ERA-Interim reanalysis data [Dee et al., 2011] show that the N-ICE2015 winter atmospheric conditions were cold compared to recent years, with mean January and February air temperatures  $-19^{\circ}\text{C}$ ,  $-9^{\circ}\text{C}$ ,  $-14^{\circ}\text{C}$ , and  $-10^{\circ}\text{C}$  for, respectively, 2015, 2014, 2013, and 2012 in the Floes 1 and 2 region (Figure 3b). The last particularly cold winter in the area was winter 2011 with mean January and February air temperature of  $-22^{\circ}\text{C}$ . The 2015 cold winter conditions in the N-ICE2015 area led to large sea ice concentrations in the region as seen in ERA-Interim data (Figure 3a). The sea ice concentrations were respectively 82%, 56%, 47%, 64%, and 97% in 2015, 2014, 2013, 2012, and 2011. Graham et al. [2017]

give a detailed comparison of the N-ICE2015 atmospheric observations with the 2015 ERA-Interim data.

#### 3.2. Hydrography and Water Masses

##### 3.2.1. Hydrographic Overview

For large parts of the drifts, the hydrography showed classic Arctic Ocean properties, with a cold, relatively fresh, and deep mixed layer in winter between 50 and 100 m thick (Figures 4a and 4b). Warmer and more salty AW was found between 200 and 800 m depth. At the end of Floes 1, 3, and 4, warmer AW was found concurring with shallower

**Table 2.** N-ICE2015 Expedition Environmental Conditions Presented as Time-Averaged Values Over Each Floe Drift<sup>a</sup>

	Floe 1	Floe 2	Floe 3	Floe 4
Drift speed ( $\text{m s}^{-1}$ )	0.16	0.21	0.14	0.21
Mean distance to open water (km)	137	239	120	43
Mean depth (m)	3485	3990	1482	1176
Mean absolute current speed below 50 m ( $\text{m s}^{-1}$ )	0.06	0.02	0.07	0.11
Mean predicted tidal currents (AOTIM-5) ( $\text{m s}^{-1}$ )	0.02	0.01	0.05	0.07
Observed tidal current amplitude ( $\text{m s}^{-1}$ )	0.06	0.02	0.08	0.10
Mean mixed-layer depth (m)	57.0	83.7	47.8	4.6
Mean mixed-layer temperature ( $^{\circ}\text{C}$ )	-1.84	-1.85	-1.81	-1.35
Mean mixed-layer salinity ( $\text{g kg}^{-1}$ )	34.43	34.50	34.34	33.52
Mean wind speed ( $\text{m s}^{-1}$ )	7	6	6	7
Mean air temperature ( $^{\circ}\text{C}$ )	-27	-14	-10	-0.4
Number of storms	5	3	8	2

<sup>a</sup>Air temperature, wind speed, and storms definitions come from Cohen et al. [2017]; definition of distance to open water in Itkin et al. [2017].

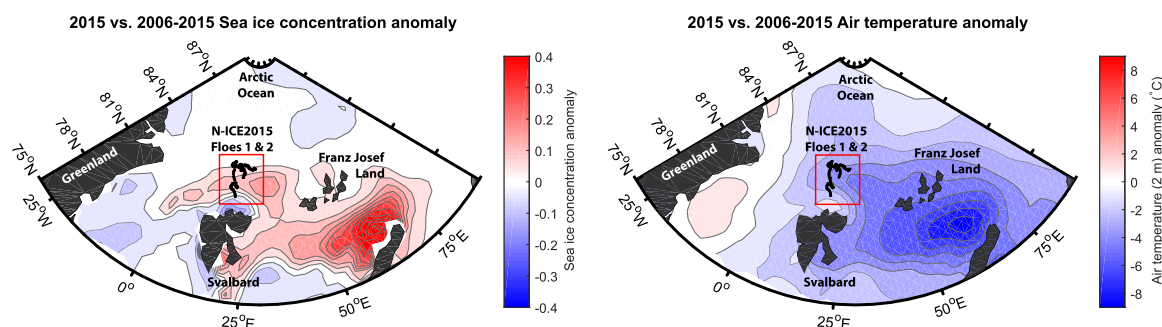


**Figure 3.** 2015 winter Sea ice concentration (a) and air temperature (b) anomalies relative to the 2006-2015 average ERA Interim reanalysis data. The red box represents the N-ICE2015 winter area.

topography (Figure 4f). Hydrographic conditions changed significantly after 25 May 2015, when water observed between 100 and 500 m depth was warmer and saltier, while the mixed layer became thinner, fresher, and warmer (Figures 4a and 4b).

### 3.2.2. Water Masses

During the drifts, six different water masses were identified using *Rudels et al.* [2000] classification (Figure 5). The water mass analysis was based on data from the ship CTD, the microstructure profilers and the IAOOS buoys profilers (Table 1).

At the surface, we found a layer of Polar Surface Water (PSW,  $\sigma_0 < 27.70$  and  $\theta < 0^\circ\text{C}$ ) throughout the N-ICE2015 expedition, on average 93 m thick in winter and 78 m thick in spring (Figures 5 and 6). Its temperature was near freezing in winter (mean  $-1.76^\circ\text{C}$ ) and higher in the spring (mean  $-1.62^\circ\text{C}$ ).

Patches of warm Polar Surface Water (PSWw,  $\sigma_0 < 27.70$  and  $\theta < 0^\circ\text{C}$ ), a signature of ice melt water, were observed in the upper 50 m during spring on the Yermak Plateau, at the end of Floes 3 and 4 (Figure 6). PSWw average temperature was  $0.9^\circ\text{C}$  and its maximum measured temperature was  $4.3^\circ\text{C}$ .

Atlantic Water (AW,  $27.70 < \sigma_0 < 27.97$  and  $\theta > 2^\circ\text{C}$ ) was observed both on the continental slope of Svalbard (Svalbard Branch) and on the Yermak Plateau (Figure 2). On the Yermak Plateau, AW was found between 100 and 500 m depth (Figure 6). AW mean temperature was  $2.7^\circ\text{C}$  and mean salinity  $35.15 \text{ kg kg}^{-1}$ , with a maximum temperature of  $4.4^\circ\text{C}$ . AW observed on or at the edge of the Yermak Plateau was defined as either of Yermak Branch origin, or undetermined branch (Figure 6). This classification is discussed in details in section 4.3. Dissolved oxygen concentrations in AW are typically the lowest observed during the expedition with values between  $280$  and  $300 \mu\text{mol kg}^{-1}$  (Figure 5b). The exception is relatively high values of dissolved oxygen ( $>320 \mu\text{mol kg}^{-1}$ ) found in the undetermined branch of AW in the southeast region of the Yermak Plateau (Figures 5b and 2, magenta drift track).

Modified Atlantic Water (MAW,  $27.70 < \sigma_0 < 27.97$  and  $\theta > 2^\circ\text{C}$ ) is the result of AW cooling and mixing with polar waters as it circulates through the Arctic (Figure 5a). MAW was found from approximately 100 m depth to 500 m unless AW was present (Figures 5 and 6).

Intermediate Water (IW,  $27.97 < \sigma_0$ ,  $\sigma_{0.5} < 30.444$  and  $\theta < 0^\circ\text{C}$ ) and Nordic Deep Water (NDW,  $\sigma_{0.5} > 30.444$ ) were found from 900 m and below in all ship CTD casts apart from over shallower parts of the Yermak Plateau (Figure 6).

### 3.3. Mixed-Layer Characteristics

The microstructure profiler data, averaged in 1 m bins, was used to derive the mixed-layer depth (Figures 7a, 4a, and 4b). In winter, the mixed-layer depth was defined as the depth in each profile where the potential density first exceeded the density at 20 m depth by  $0.01 \text{ kg/m}^3$ . In spring, we found the depth in each profile where the potential density first exceeded the surface (second good data point usually at 2 m depth) density by  $0.003 \text{ kg/m}^3$ . The lower density criteria used for spring was used to avoid overestimating the mixed-layer depth since the density gradient at the base of the mixed layer was smaller in spring than in winter. Overall, the mixed-layer depth estimates are not sensitive to the choice of density criteria, which are adjusted for the spatial and temporal coverage of data. Criteria definitions are typical for the Arctic region [Peralta-Ferriz and Woodgate, 2015].



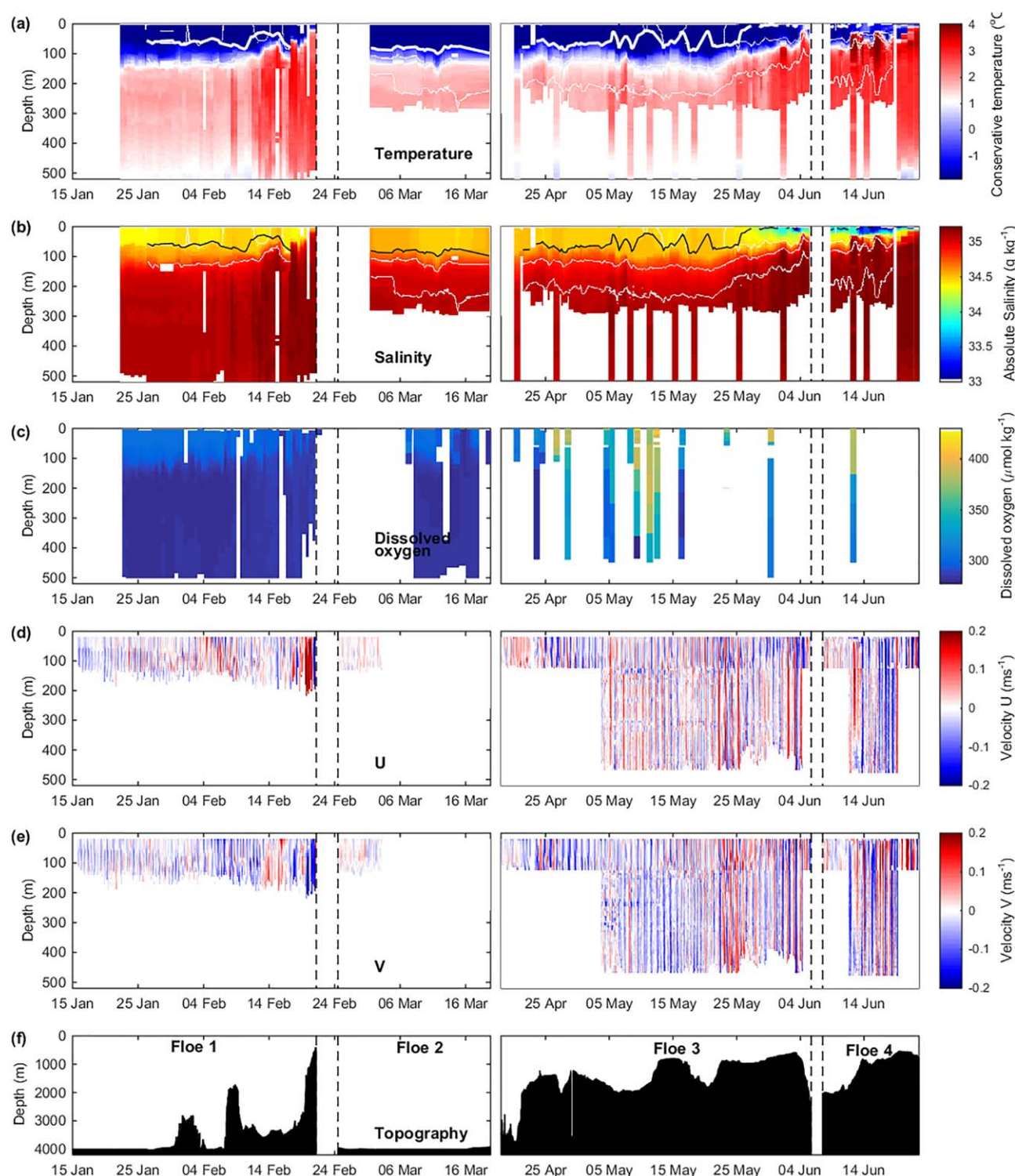


**Figure 4.** Vertical distribution of (a) conservative temperature and mixed-layer depth (thick white line), (b) Absolute Salinity and mixed-layer depth (thin black line), (c) dissolved oxygen, (d) zonal (U) and (e) meridional (V) component of the absolute current velocity, and (f) seafloor depth along the N-ICE2015 drifts trajectories. In (a) and (b), data above 300 m is from microstructure profilers and data below is from ship CTD, apart from Floe 1 where upper 200 m are microstructure profilers and below 200 m is IAOOS profilers. In (c), data is from IAOOS profilers for Floe 1 and from either ship CTD (profiles deeper 1000 m), or from the on-ice CTD (profiles shallower than 1000 m) for Floe 2, 3, and 4. In (d) and (e), data above 130 m is from the vessel-mounted ADCP while data below 130 m is from the Long-Range ADCP. White isolines correspond to selected potential density contours: 27.6, 27.8, and 27.9  $\text{kg m}^{-3}$ . Vertical dashed lines separate drifts.

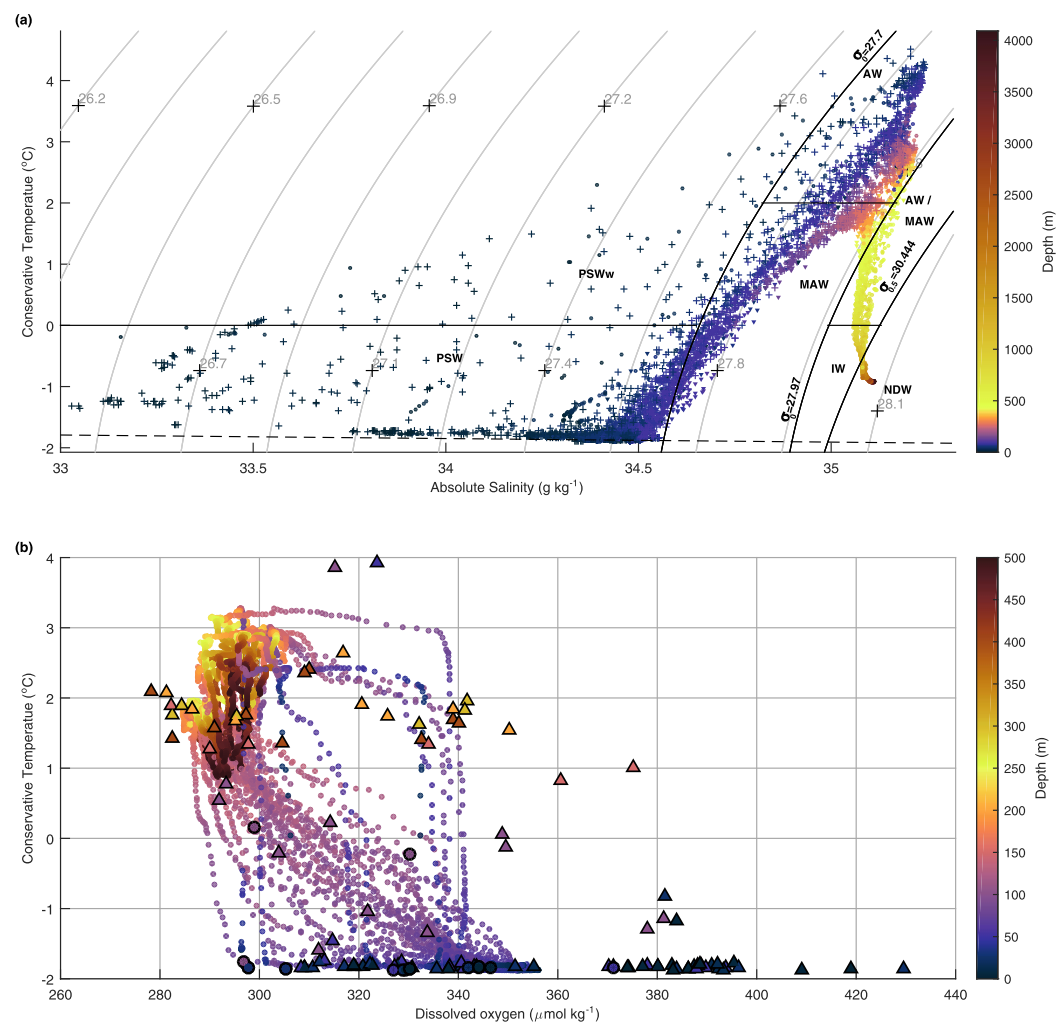


**Figure 5.** (a) Conservative temperature versus Absolute Salinity from ship CTD data (dots) and from microstructure profiler data (crosses) color-coded for observation depth. Definitions of water masses following Rudels *et al.* [2000] are indicated: Atlantic Water (AW), Modified Atlantic Water (MAW), Polar Surface Water (PSW), Warm Polar Surface Water (PSWw), Intermediate Water (IW), and Nordic Deep Water (NDW). The dashed line corresponds to the freezing point of seawater. (b) Conservative temperature versus dissolved oxygen from bottle CTD data (large dots and triangles) and from IAOOS profiler data (small dots). Color indicates the depth of each sample, all dots are winter samples, and triangles are spring samples.

The mean conservative temperature and Absolute Salinity within the mixed layer were derived and the local freezing temperature was calculated at 2 m depth. A measure of the vertical temperature gradient at the base of the mixed layer was derived applying a linear least square fit of conservative temperature values in the 5 m section directly below the base of the mixed layer (Figure 7b) [Toole *et al.*, 2010]. We also defined the departure from freezing temperature ( $\delta T$ ) as the difference between the mean temperature in the mixed layer and the local freezing temperature  $\delta T = T - T_f(S, p)$  (Figure 7c).

The mean mixed-layer depth for the expedition was 44 m with values ranging from 1 to 100 m (Table 2 and Figure 7a). The deepest mixed layers were observed in March and the shallowest in June. In winter, the mixed layer was close to freezing with  $\delta T = 0.03^\circ\text{C}$ . During Floe 3,  $\delta T$  doubled to  $0.06^\circ\text{C}$  and it reached very large values in June with a mean of  $0.47^\circ\text{C}$  during Floe 4. The temperature gradient at the base of the mixed layer was occasionally negative in the late spring (end of Floes 3 and 4) as a result of strong vertical interleaving in the upper 80 m of the water column.

A dramatic change was seen in mixed-layer characteristics after 25 May, while the camp was drifting over the Yermak Plateau. Prior to the 25 May, the mixed layer was deep (average of 64 m) and close to the freezing point. After the 25 May, a different mixed layer was encountered. It was very shallow (average of 6 m)

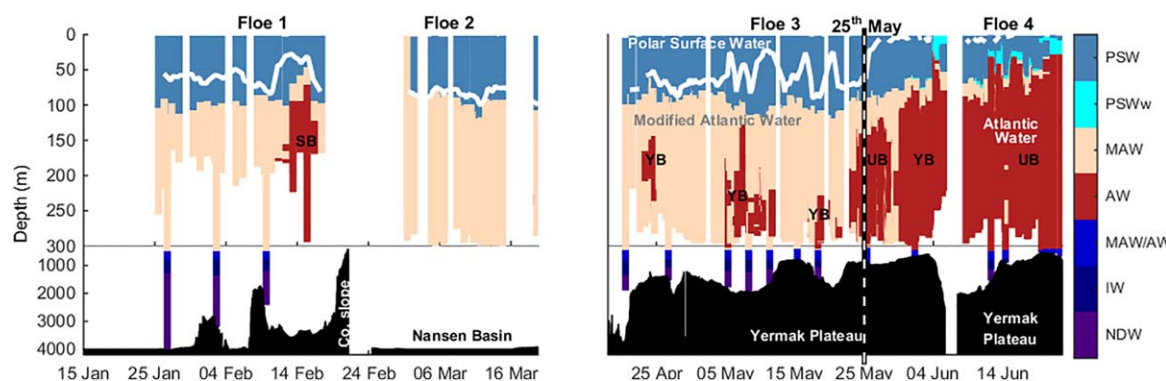


**Figure 6.** Vertical distribution of water masses along the N-ICE2015 drift trajectory. Water-masses are labeled by color: Atlantic Water (AW), Modified Atlantic Water (MAW), Polar Surface Water (PSW), Warm Polar Surface Water (PSWw), Intermediate Water (IW), and Nordic Deep Water (NDW) following Rudels *et al.*'s [2000] definitions. Patches of Atlantic Water are indicated coming from either the Svalbard Branch (SB), the Yermak Branch (YB), or undetermined (UB). The vertical scale is zoomed in the upper 300 m. The date of 25 May 2015 is indicated by a thick vertical black and white dashed line. Overlying the water masses color scale is a contour of the mixed-layer depth (white line). The corresponding depth (m) of the seafloor along the N-ICE2015 drift trajectory shows topographic features (black).

and had temperatures significantly above freezing. A remnant winter mixed layer was still present below the newly formed mixed layer for some time. The vertical temperature gradient at the base of the mixed layer also showed a shift on the 25 May with a mean value prior to this date of  $0.25^{\circ}\text{C m}^{-1}$  that dropped to  $0.01^{\circ}\text{C m}^{-1}$  afterward. Large basal sea ice melt events took place after 25 May driven by large ocean heat flux from Atlantic Water [Peterson *et al.*, 2017; Meyer *et al.*, 2017], leading to a freshening of the upper surface waters, an increase in buoyancy, and was likely responsible for the new shallow mixed layer.

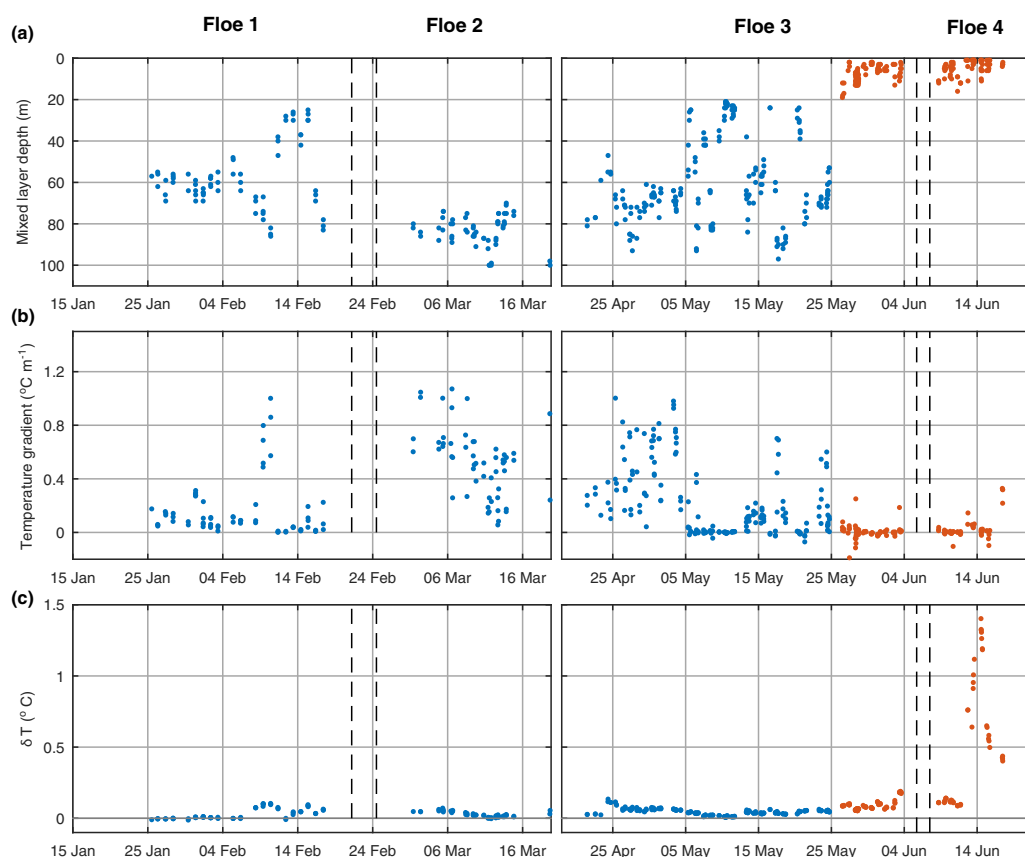


**Figure 7.** Time evolution during the N-ICE2015 expedition of (a) the mixed-layer depth, (b) the vertical conservative temperature gradient in the 5 m below the mixed-layer base, and (c) the mean mixed-layer temperature departure from freezing point ( $\delta T = T - T_f(S, p)$ ) before 25 May 2015 (blue) and after 25 May 2015 (brown), from individual microstructure profiles.

### 3.4. Seasonal and Regional Variability

#### 3.4.1. In the Observations

Winter drifts (Floes 1 and 2) were in waters on average deeper than 3000 m, with a deeper mixed layer and cooler waters throughout the water column (Table 2). Winter waters were depleted in dissolved oxygen compared to concentrations in the spring (Figure 4c).

The spring drifts (Floes 3 and 4) were in shallower waters, with a shallower mixed layer, warmer waters and higher air temperatures (Table 2). Dissolved oxygen profiles in the spring showed enhanced values in the upper 100–400 m (Figure 4c).

We further split the spring data in two periods: early spring (until 25 May 2015) and late spring (after 26 May 2015) based on changes observed in temperature and salinity at that time (Figure 6, thick black and white dashed line). The winter and early spring mean vertical profiles of temperature, salinity, and density were near identical (Figures 8a–8c). The mean winter dissolved oxygen profile showed a strong gradient from surface values of 340 to 290  $\mu\text{mol kg}^{-1}$  at 200 m depth and below (Figure 8d). The late spring profiles, however, were very different from the winter profiles with warmer waters from surface down to 500 m, much fresher and lighter waters in the upper 50 m and saltier waters between 50 and 600 m depth. This corresponded to the presence of AW at depth. We do not have sufficient data on dissolved oxygen during spring to discuss changes during that period.

During the expedition, two areas were sampled twice: The northern tip of the Yermak Plateau was first sampled during Floe 1 (31 January to 3 February) and then revisited about three months later during Floe 3 (20–22 April). The south-west edge of the Plateau was sampled at the end of Floe 3 (28 May to 4 June) and again 17 days later at the end of Floe 4 (13–20 June) (Figure 2). We compared temperature and salinity data for both regions over time and found that changes from winter to spring on the northern tip of the Plateau were very small (Figure 8i, green and yellow colors). Only in the upper 40 m, we observed slightly fresher waters in winter ( $-0.06 \text{ g kg}^{-1}$ ). Changes from late May to mid-June in the southwest part of the Plateau later were also small (Figure 8i, pink and purple colors). In June, AW was warmer and PSW was fresher than in May. This coincided with the June drift being closer to open water than the May drift.

Three bathymetric areas are defined for the N-ICE2015 data set: deep topography, deeper than 3000 m, corresponding to the Nansen Basin, slope area between 3000 m and 1500 m depth, and shallow topography, shallower than 1500 m, which corresponds mainly to the Yermak Plateau and partly to the upper continental slope at the end of Floe 1 (Figure 2). From deep to shallow topography, we saw a transition from PSW and MAW to PSWw and AW: waters became warmer from the surface down to 500 m depth, fresher and lighter at the surface, and saltier at depth (Figures 8e–8g). There was a strong deficit in dissolved oxygen concentrations in the upper layer (0–100 m) of the shallow profiles with a maximum difference in surface values of 310  $\mu\text{mol kg}^{-1}$  compared to 340  $\mu\text{mol kg}^{-1}$  in deeper profiles (Figure 8h).

Dissolved oxygen values were lower in winter and in shallow waters. Low-dissolved oxygen values in winter under the sea ice are expected since such regions have been isolated from the atmosphere for several months and minimal primary production takes place in that period. In shallow waters, low surface levels of dissolved oxygen could be due to significant remineralization over the continental shelf and exchanges between the mixed layer and AW due to enhanced mixing on the slope. Higher upper ocean dissolved oxygen values observed in the spring are likely the result of oxygen exchanges with the atmosphere through leads in the sea ice (ventilation) and biological production of oxygen in the water (photosynthetic activity) due to increased under ice light levels [Timmermans *et al.*, 2010]. Such photosynthetic activity was observed with an under-ice phytoplankton bloom taking place in May and June 2015 during the expedition [Assmy *et al.*, 2017].

#### 3.4.2. Comparison With Ocean Climatology

The observations and derived MIMOC interpolated profiles of climatology (section 2.4.1) are binned in three time periods: winter for data between January and March; early spring for data between April and May and late spring for data in June. The number of profiles the climatology is based on in January is small (less than ten) for the N-ICE2015 January region (Figure 9a). This number increases to approximately 40 profiles in March, and to over 70 profiles in May (Figures 9b and 9c).

The key feature we found comparing the N-ICE2015 observations with the MIMOC ocean climatology was that the upper Atlantic Water layer is warmer, more saline and shallower in the new observations compared to the climatology, throughout the N-ICE2015 expedition (Figures 9d–9i). The signal of higher



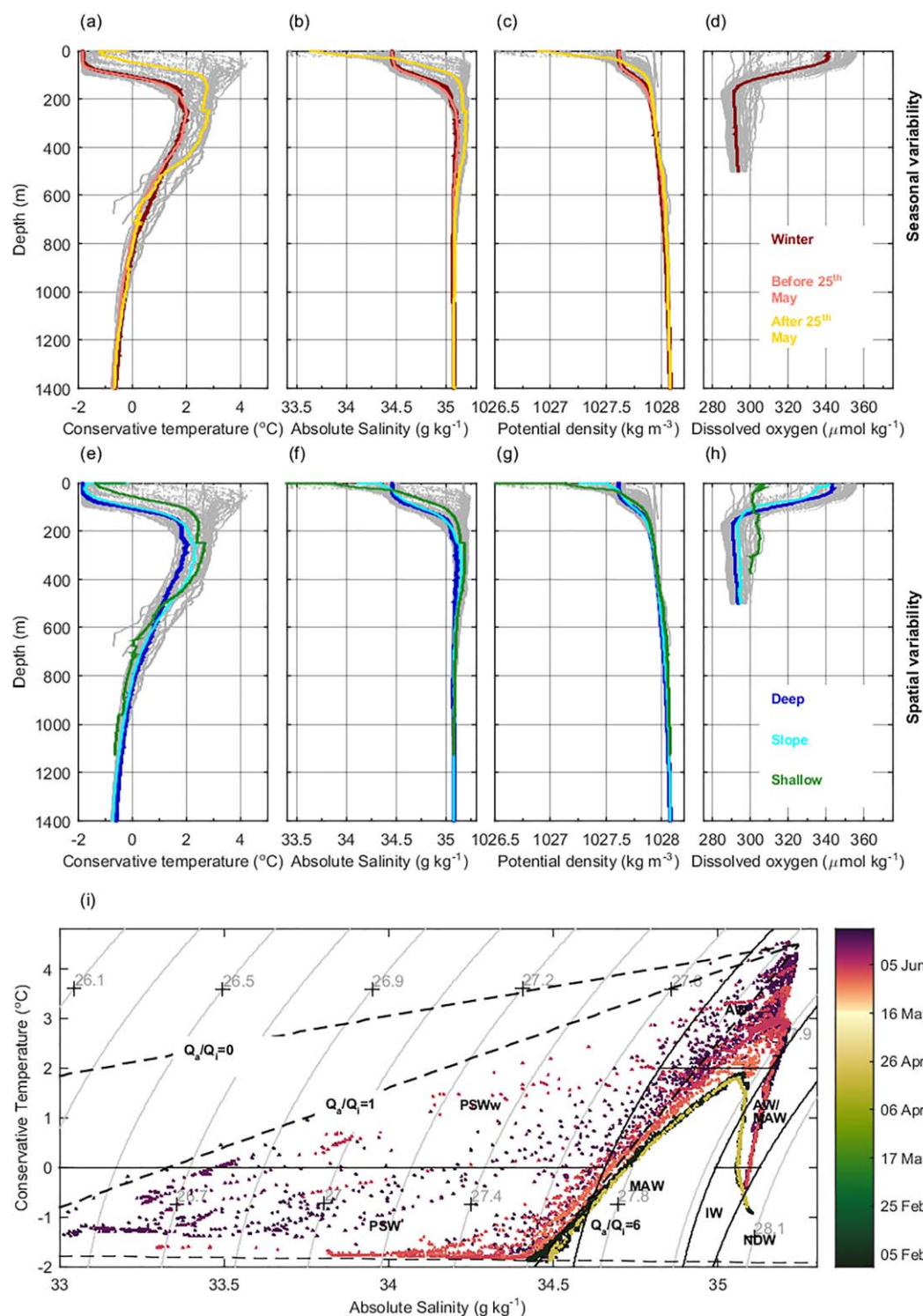


**Figure 8.** Mean vertical profiles of (a and e) conservative temperature, (b and f) Absolute Salinity, (c and g) potential density, and (d and h) dissolved oxygen. In Figures 8a–8d, data are averaged by seasons where winter is from 15 January to 19 March (red line), early spring is from 18 April to 25 May (pink line) and late spring is from 26 May to 22 June (yellow line). In Figure 8e–8h, data are averaged by location where deep is deeper than 3000 m (dark blue line), slope is between 3000 m (cyan line) and 1500 m depth and shallow is shallower than 1500 m (green line). (i) Conservative temperature versus Absolute Salinity from ship CTD data and from microstructure profiler data. Colors indicate the dates at which data were sampled: Dark green and yellow points are from the northern tip of the Yermak Plateau in January and April respectively; pink and purple points are from the south-west edge of the Plateau in May and June respectively. Black dashed lines show various values of the atmospheric cooling ( $Q_a$ ) to ice melt ( $Q_i$ ) ratio. In Figures 8a–8c, 8e, 8f, and 8g, data above 300 m is from microstructure profilers while data below 300 m is from the ship CTD. In Figures 8d and 8h, data are from the IAOOS profilers (Floe 1 only).



temperature and salinity is seen between 100 and 220 m depth in the Nansen Basin and on the northern section of the Yermak Plateau, while it reaches as deep as 500 m depth on the southern section of the Yermak Plateau.

Another clear difference is the higher salinity of surface waters in winter and early spring (Figures 9e and 9g, upper 40 m). Such high salinities could be due to stronger local sea ice formation during winter 2015 than in previous years, leading to brine release in the upper water column. In the late spring, the warm shallow AW led to sea ice melt [Meyer *et al.*, 2017] and a pronounced drop in subsurface salinities in the observations. Here the climatology does not capture this surface melt water signal and observed salinity in the upper 30 m is much lower than in the climatology.

### 3.4.3. Cold Halocline and Sea Ice

The upper mixed layer in the observations is more saline than the climatology, a sign of more sea ice formation in the region, consistent with measurements of divergent sea ice motion during winter storms of the N-ICE2015 expedition [Itkin *et al.*, 2017]. Indeed, large sea ice divergence events suggest that leads opened in the ice. This would have led to high sea ice growth rates under the anomalous low atmospheric temperatures. The deep mixed layer observed could be the result of deep convection following strong freezing and resulting brine release.

The shape of temperature versus salinity profiles is associated with surface heat loss due to atmospheric cooling and to ice melting [Boyd and D'Asaro, 1994; Cokelet *et al.*, 2008]. The temperature and salinity slopes of constant atmospheric cooling ( $Q_a$ ) to ice melt ( $Q_i$ ) were derived using

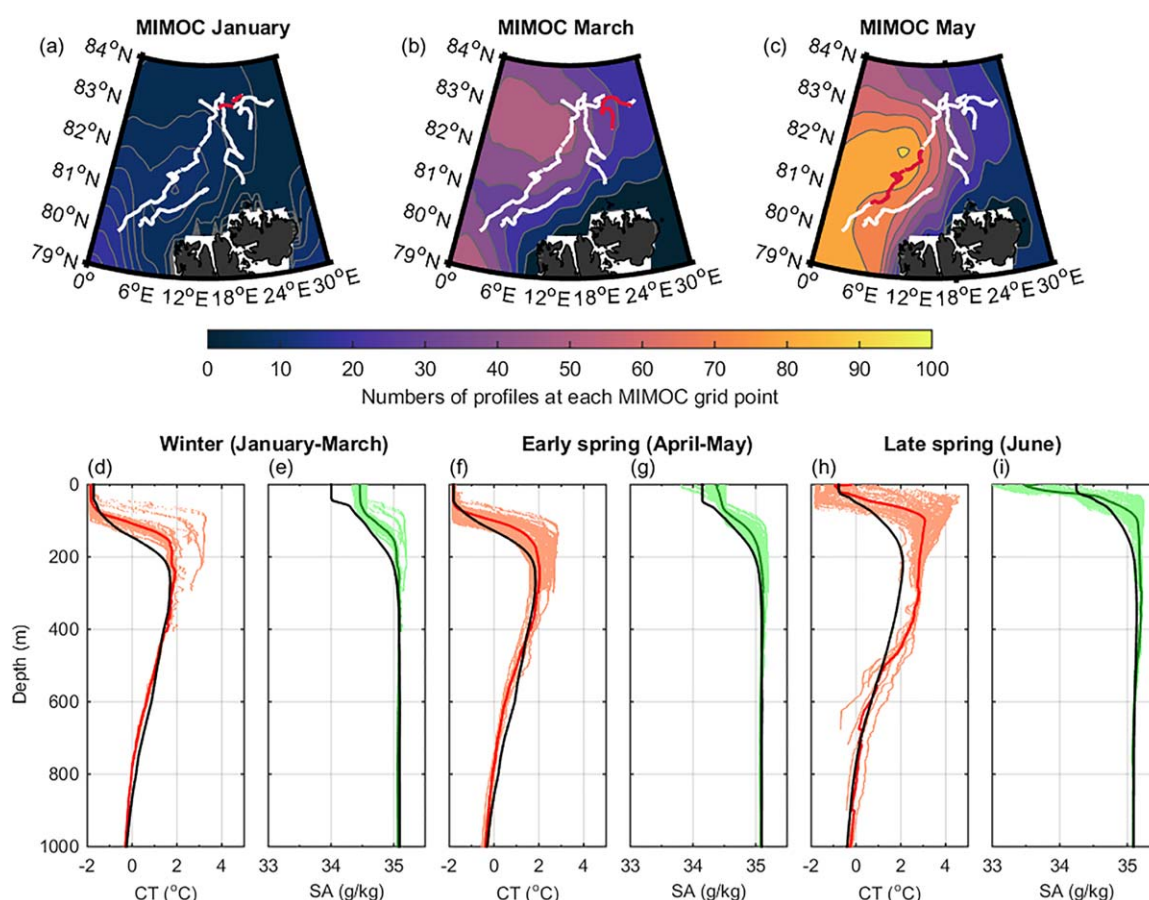


**Figure 9.** (a) Maps with the number of profiles at each grid point of the MIMOC climatology for the month of January with contour intervals every two profile, (b) March with contour intervals every 10 profile, and (c) May with contour intervals every 10 profile. Overlay in white are the drift tracks of the N-ICE2015 expedition and in red the respective drift sections for the shown month. Mean vertical profiles of conservative temperature (CT) and Absolute Salinity (SA) from the N-ICE2015 expedition observations (color) and from MIMOC climatology (black), (d and e) for winter, (f and g) early spring, and (h and i) late spring. Data above 300 m include microstructure profilers and ship-board CTD. Data below 300 m is from the ship-board CTD only.

$$T = T_0 + 79.2 \left( 1 + \frac{Q_a}{Q_i} \right) \ln \left( \frac{S - S_i}{S_0 - S_i} \right), \quad (1)$$

where  $T_0 = 4.5^\circ\text{C}$  and  $S_0 = 35.25 \text{ g kg}^{-1}$  represent the virtual AW maximum, and  $S_i = 5$  is an assumed sea ice salinity [Cokelet *et al.*, 2008]. These slopes are appropriate for surface waters where atmospheric cooling and sea ice melt take place. The  $Q_a/Q_i = 0$  slope theoretically corresponds to no atmospheric sensible heat transfer and large sea ice melt (Figure 8i). The N-ICE2015 late spring temperature and salinity data had  $Q_a/Q_i$  ratios as low as 1 (Figure 8i), consistent with both ice melting and heat loss to the atmosphere taking place. In winter and early spring however, the  $Q_a/Q_i$  ratio was approximately 6, indicative of Polar Surface Water formation with very little ice melt taking place.

### 3.5. Surface Currents and Drift

Drift speed of the ice camps throughout the expedition averaged  $0.17 \text{ m s}^{-1}$  with peaks above  $0.50 \text{ m s}^{-1}$  (Figure 10a). The overall drift direction was south-west towards Fram Strait. The sea ice drift is determined by a combination of wind forcing, sea ice stresses and ocean forcing (tides and currents). During the N-ICE2015 expedition, the wind component was largest when the ice camps were closest to the ice edge (Floes 3 and 4) [Peterson *et al.*, 2017]. When drifting deeper inside the pack ice (Floes 1 and 2), internal sea ice stress and oceanic forcing dominated.

Stronger mean ocean currents were generally recorded at the end of each drift when the ice camp approached the sea ice edge, shallower bathymetry, and the AW inflow. Figure 10 shows this increase in current speed when the distance to open water decreases, and when AW is present at depth (Figure 10c).

Most of the observed peaks in drift speed (Figure 10a) were clearly associated with the passage of atmospheric low pressure events, recorded as storms [Cohen *et al.*, 2017]. The storms also appear to have influenced the observed mean absolute current speeds in the upper 23–55 m (Figure 10b). When drift speed exceeded  $0.4 \text{ m s}^{-1}$ , mean current speed in the upper 55 m rose from an average  $0.06\text{--}0.12 \text{ m s}^{-1}$ . Large upper ocean mean current speeds nearly always matched storm events, apart from a period after 17 June at the end of the N-ICE2015 expedition. After that date, large drifting speeds were associated with large upper ocean current speeds but with no corresponding storm. That period corresponded to the largest predicted and observed tidal signal suggesting that the large current and drift speeds were tide driven.

### 3.6. Deeper Circulation

Observed absolute mean current speeds below 50 m depth varied from a minimum of  $0.02 \text{ m s}^{-1}$  with direction rotating with tides in the Nansen Basin during Floe 2, to quite high values above  $0.20 \text{ m s}^{-1}$  flowing north-east on the Svalbard continental shelf during Floe 1. In the south-western part of the Yermak Plateau current speed was moderate with westwards and north-west direction;  $0.11 \text{ m s}^{-1}$  during Floe 3 and  $0.17 \text{ m s}^{-1}$  during Floe 4 (Figures 4d and 4e). Data from the two ADCPs showed barotropic flow with little vertical variability in the velocity profiles (Figures 4d and 4e). Some exceptions were observed following atmospheric storm events and on the Svalbard continental slope (not shown).

Overall, the ocean flow below 50 m depth was westwards and north-west in the south-west area of the Yermak Plateau close to the slope. At the northern tip of the Yermak Plateau, the mean current curled around the tip of the plateau (Figure 11d). Along the eastern slope of the Plateau, the consistent weak south, south-west current had a mean speed of  $0.06 \text{ m s}^{-1}$ . Finally, a strong north-east flowing current signal was observed on the upper Svalbard continental slope (Figures 11a–11c). With corresponding AW characteristics (Figure 11b), this strong current was the Svalbard Branch of the AW inflow with a narrow core found below 50 m depth and reaching at least down to 200 m depth (Figure 11b). This core had an average current speed of  $0.25 \text{ m s}^{-1}$  located above the 600 and 900 m isobaths.

### 3.7. Tides and Oscillations

Tidal current predictions were estimated along the four drifts using the AOTIM-5 model (Figures 12a and 12b, red curves). Current signals at tidal frequencies (24 and 12 h) were estimated using the vessel-mounted ADCP data (Figures 12a and 12b, blue curves). Tidal signals were weak in the Nansen Basin with both observed and predicted average current values of  $0.02 \text{ m s}^{-1}$  (Table 2). Tides on the Yermak Plateau and on its slopes were relatively strong and dominated the current signal (Figure 11a, red areas), with observed current signals at tidal frequencies reaching  $0.42 \text{ m s}^{-1}$ .

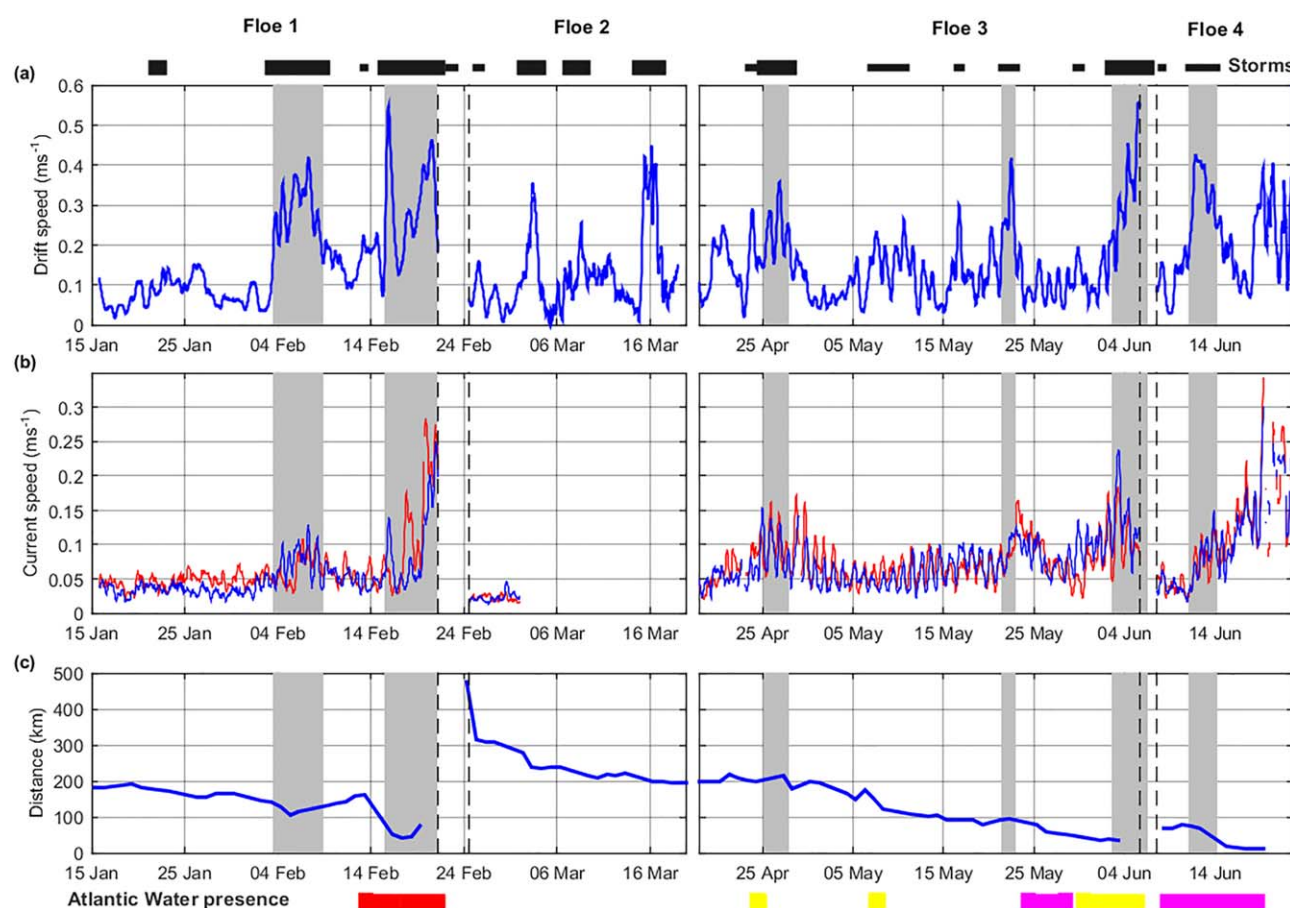


**Figure 10.** Time evolution during the N-ICE2015 expedition of (a) the drift speed of the ice, (b) mean absolute current speed (vessel-mounted ADCP data) in the upper 23–55 m (blue) and mean absolute current speed in the 100–150 m depth range (red), and (c) distance from the drifting ice floe to open water [Itkin *et al.*, 2017]. Black blocks indicate major storms (thicker boxes) and minor storms (thinner boxes) [Cohen *et al.*, 2017]. Presence of Atlantic Water in the water column is indicated and labeled from either the Yermak Branch (yellow blocks), from undetermined origin (magenta blocks), or from the Svalbard Branch (red blocks). Storm events associated with large drift speeds and increased observed current speeds are highlighted in gray across the plots. Note that the vessel-mounted ADCP was non-operational after the 3 March 2015 during drift 2 when the ship bow was lifted out of the water by sea ice compression events.

The phase of the predicted tides matched observed signals well, and the amplitudes of observed and predicted tidal signal were comparable during Floe 2, for the end of Floe 3 and for Floe 4. The amplitude of the observed signals was however larger than predicted tides during Floe 1 and during the first part of Floe 3 (Table 2). The difference might be due to predicted tidal signal being underestimated by the AOTIM-5 model. For example, its bathymetry may be inaccurate as it does not incorporate recently collected data and its resolution is coarse (5 km). This particularly affects tidal estimates near slopes and in coastal regions.

#### 4. Discussion

The new observations from the N-ICE2015 expedition have long lasting potential to improve our understanding of the processes governing the Arctic Ocean during winter. N-ICE2015 was able to collect more than 250 winter CTD casts from ship CTD, microstructure profiles, and buoys, in a region with extremely sparse winter data coverage (Figure 9a). N-ICE2015 creates an unprecedented basis for studies on Arctic ocean winter processes and thus is crucial to reduce bias for modelling future Arctic conditions. This region is in a transition period, with basin wide sea ice thickness reduced from 3.60 to 1.25 m between 1975 and 2012 [Lindsay and Schweiger, 2015]. The general trend of thinning sea ice in the Fram Strait area is similar to that in the wider Arctic Ocean [Renner *et al.*, 2014], and given that sea ice in the Yermak Plateau area generally drifts from the interior basin towards Fram Strait, a similar trend is also expected there. However, larger variability is observed north of Svalbard [Renner *et al.*, 2013], likely associated with a larger fraction of first-year ice in this region.



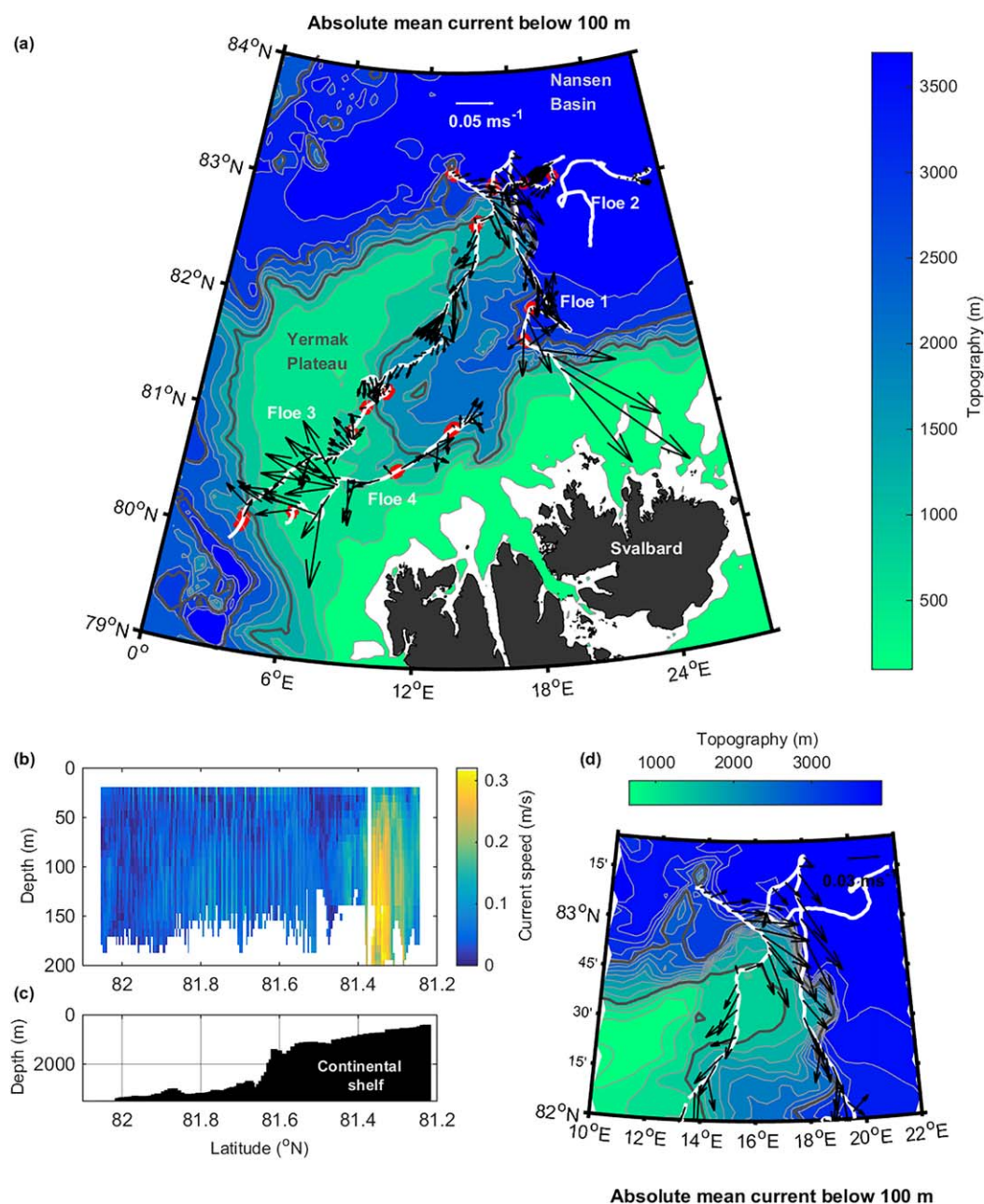


**Figure 11.** (a) Mean absolute ocean currents below 100 m depth from available Vessel-Mounted ADCP data overlaying topographic contours ranging from 100 to 4000 m at 400 m intervals (color). Red sections along drift tracks correspond to areas where estimated tidal speed dominates observed absolute current speed. (b) Section plot of residual current speed while drifting onto the continental shelf at the end of Floe 1 (Vessel-Mounted ADCP data). (c) Corresponding underlying topography. (d) Mean absolute currents at the northern tip of the Yermak Plateau below 100 m depth from available Vessel-Mounted ADCP data overlaying topographic contours at 200 m intervals (color). In both (a) and (d), the 3000 and 1500 m isobaths are shown as thick gray lines while the trajectories of Floe 1 and 3 are indicated with white lines.

#### 4.1. Upper Layer Characteristics and Formation of the Cold Halocline

Our observations are consistent with the general description of dominating processes in the area. Nowadays, the region north of Svalbard likely receives a thinner sea ice cover by predominantly wind driven sea ice transport [Hansen et al., 2013; Renner et al., 2013, 2014; Lindsay and Schweiger, 2015]. Snow-free and thinner sea ice would allow for further growth in particular during cold winters, despite the relatively large ocean heat flux in the region [Peterson et al., 2016, 2017; Meyer et al., 2017]. Snow cover was however thick during N-ICE2015 [Merkouriadi et al., 2017; Rösel et al., 2016] insulating the ice from the atmosphere and

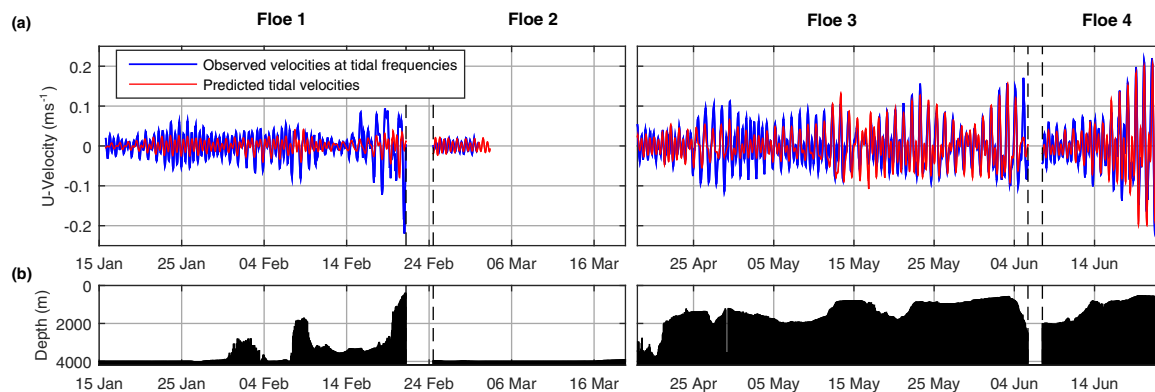


**Figure 12.** Time evolution during the N-ICE2015 expedition of (a) Observed U-velocities of waves with 12 and 24 h frequencies between 100 and 250 m depth from vessel-mounted ADCP data (blue) and predicted tidal velocities from AOTIM-5 (red). V-velocities (not shown) are similar. (b) Corresponding depth (m) of the seafloor along the N-ICE2015 drift trajectory.

preventing sea ice growth (A. Rösel, personal communication, September 2016). It is instead in the many observed leads that strong thin ice growth was observed. A negative feedback loop might then come into effect where sea ice growth drives vertical convection, bringing up more of the Atlantic Water heat to the sea ice, preventing its growth [Ivanov *et al.*, 2016].

#### 4.2. Atlantic Water Characteristics and Circulation

On the western side of the Yermak Plateau, AW observed from 30 m depth with 2.8°C mean temperature is identified as part of the Yermak Branch of inflowing AW (Figure 2, yellow drift track). At the northern end of the Yermak Plateau, currents were consistently observed curling around the tip of the Plateau, when the ice camps drifted across both in winter and in spring (Figure 11d). Concurrently, AW was observed from 130 m depth, with 2.1°C mean temperature above the 1500 m isobaths (Figure 2), similar characteristics to those observed by Rudels *et al.* [2005]. We identify this section as the Yermak Branch retroflecting around the northern tip of Yermak Plateau. Further downstream, along the eastern side of the Yermak Plateau, AW was observed again at, respectively, 128 and 230 m depth, with mean temperatures of 2.3 and 2.0°C C over the 1900 and 1600 m isobaths (Figure 2). With absolute current speeds that were consistently south along that section (Figure 11a), we identify this section as the Yermak Branch that has cooled down and eroded after circulating around the Yermak Plateau. This is similar to previous findings in the area [Rudels *et al.*, 2000; Marnela *et al.*, 2013]. What happens to the Yermak Branch south of 81° latitude on the eastern side of the Plateau is unclear. AW is observed again on the Plateau and on its eastern slope but this AW is much shallower (120 and 30 m depth), much warmer (2.8 and 3°C) and over shallower topography (900 and 1200 m isobaths) (Figure 2, magenta drift track). Current speeds in the area are low and tidal dominated (Figure 11a). This AW, referred to as the undetermined branch (Figure 6), could be coming from the Yermak Branch through the Yermak Plateau Pass taking a short-cut across the Plateau [Gascard *et al.*, 1995]. Alternatively, this AW could have “leaked” from the Svalbard Branch, with eddies [Våge *et al.*, 2016; Koenig *et al.*, 2017] and slowly accumulated in that area.

The Svalbard branch of inflowing AW was clearly observed in the ocean current observations between the 600 and 1000 m isobaths at 81.5°N (Figures 11b and 2, red track). The observed distribution and T-S characteristics of AW over this part of the continental slope was very similar to that found by Cokelet *et al.* [2008]. They calculated geostrophic currents in the AW core of order 5 cm<sup>-1</sup>, significantly lower than the 25 cm<sup>-1</sup> measured during N-ICE2015. Apart from differences between geostrophic estimates and direct measurement, this difference could be due to short-term variability as well as seasonality of the inflow; based on mooring records, Randelhoff *et al.* [2015] show that the Svalbard Branch is stronger in winter (N-ICE2015 observations) and spring than in summer and autumn [Cokelet *et al.*, 2008, observations]. Similar seasonal variability of the Svalbard Branch is presented in Koenig *et al.* [2017].

Even though AW has been shown to have a hydrographic seasonal cycle [Schauer *et al.*, 2002; Ivanov *et al.*, 2009], this data set does not allow for such analysis. The changes in temperature and salinity observed during the N-ICE2015 expedition seem to be dominated by the presence of AW on the slopes and over the



Yermak Plateau. Changes from winter to spring near the northern part of the Plateau were near to none and restricted to the upper 40 m, while changes on the south-west edge of the Plateau seemed driven by the location of AW and distance to the ice edge (Figure 8i).

Overall, AW was observed close to the surface under the sea ice when within 100 km from open ocean. This is consistent with the idea that warm AW in this area defines the ice boundary by providing heat to and therefore melting the sea ice from below [Untersteiner, 1988]. A comparison with climatology data shows a warmer, shallower, and more saline AW during N-ICE2015. This could point either to a higher than usual inflow of AW in early 2015, or to a continuation of the signal of the previously reported warming trend of AW inflow in the Svalbard region [Grotefendt et al., 1998; Schauer et al., 2004; Ivanov et al., 2009; Polyakov et al., 2012; Beszczynska-Möller et al., 2012].

## 5. Conclusions

The N-ICE2015 expedition data set spanning January to June 2015 provides an updated picture of the hydrography and circulation in the Arctic Ocean north of Svalbard. In addition, these rare winter data are valuable to the community with the potential to reduce bias when modelling the new Arctic. The new observations show a surprisingly deep mixed layer for the first five months of the N-ICE2015 expedition likely due to high sea ice growth rates in numerous leads, a characteristic of the area [Willmes and Heinemann, 2016]. Because few earlier observations are available, it is not possible to conclude whether this is unusual and a result from the “new Arctic” with a thinner sea ice cover, or if this has been the typical state for this region in past decades. Late spring conditions, closer to the ice edge are dominated by a strong pycnocline and shallow mixed layer, the result of large sea ice melt events.

We find that the Atlantic Water inflow north of Svalbard was warmer, more saline and shallower in 2015 than in available climatology data. The inflow is steered by topography, partly flowing along the Svalbard coast (Svalbard Branch), and partly flowing around the Yermak Plateau (Yermak Branch), shown for the first time to retroflect around its northern tip. The Atlantic Water present on the Yermak Plateau is associated with a shallow mixed layer and low sea ice concentrations. In the deep basin, Atlantic Water is found further down in the water column.

In the late spring, it is likely that the combination of strong tides, warm Atlantic Water and a shallow mixed layer during the N-ICE2015 expedition led to local enhanced heat fluxes from the ocean to the sea ice with significant implications for the sea ice energy budget.

## References

- Aagaard, K., and P. Greisman (1975), Toward new mass and heat budgets for the Arctic Ocean of major estimate of Coillin, *J. Geophys. Res.*, 80(27), 3821–3827, doi:10.1029/JC080i027p03821.
- Aagaard, K., A. Foldvik, and S. R. Hillman (1987), The West Spitsbergen Current: Disposition and water mass transformation, *J. Geophys. Res.*, 92(C4), 3778–3784.
- Abrahamsen, E. P. (2014), Sustaining observations in the polar oceans, *Philos. Trans. R. Soc. London A*, 372(2025), 20130337, doi:10.1098/rsta.2013.0337.
- Amante, C., and B. Eakins (2009), ETOPO1 1 arc-minute global relief model: Procedures, data sources and analysis, *NOAA Tech. Mem. NESDIS NGDC-24* (March), 19 pp., Natl. Oceanic and Atmos. Admin., Boulder, Colo., doi:10.1594/PANGAEA.769615.
- Assmy, P., et al. (2017), Leads in the Arctic pack ice enable early phytoplankton blooms below snow-covered sea ice, *Scientific Reports*, doi:10.1038/srep40850, in press.
- Beszczynska-Möller, A., E. Fahrbach, U. Schauer, and E. Hansen (2012), Variability in Atlantic water temperature and transport at the entrance to the Arctic Ocean, 1997–2010, *ICES J. Mar. Sci.*, 69, 852–863, doi:10.1093/icesjms/fss056.
- Bourke, R. H., A. M. Weigel, and R. G. Paquette (1988), The westward turning branch of the West Spitsbergen Current, *J. Geophys. Res.*, 93(C11), 14,065–14,077, doi:10.1029/JC093iC11p14065.
- Boyd, T. J., and E. A. D'Asaro (1994), Cooling of the West Spitsbergen Current: Wintertime observations west of Svalbard, *J. Geophys. Res.*, 99(C11), 22,597–22,618.
- Carmack, E. C., et al. (2015), Towards quantifying the increasing role of oceanic heat in sea ice loss in the New Arctic, *Bull. Am. Meteorol. Soc.*, 96(12), 2079–2105, doi:10.1175/BAMS-D-13-00177.1.
- Carpenter, J. H. (1965), The Chesapeake Bay Institute technique for the Winkler dissolved oxygen method, *Limnol. Oceanogr.*, 10(1), 141–143, doi:10.4319/lo.1965.10.1.0141.
- Cohen, L., S. R. Hudson, V. P. Walden, R. M. Graham, and M. A. Granskog, (2017), Meteorological conditions in a thinner Arctic sea ice regime from winter through summer during the Norwegian young sea ICE expedition (N-ICE2015), *J. Geophys. Res. Atmos.*, doi:10.1002/2016JD026034, in press.
- Cokelet, E. D., N. Tervalon, and J. G. Bellingham (2008), Hydrography of the West Spitsbergen Current, Svalbard Branch: Autumn 2001, *J. Geophys. Res.*, 113, C01006, doi:10.1029/2007JC004150.

## Acknowledgments

This work has been supported by the Norwegian Polar Institutes Centre for Ice, Climate and Ecosystems (ICE) through the N-ICE project. Additional support was obtained from the Centre for Climate Dynamics at the Bjerknes Centre through grant BASIC: Boundary Layers in the Arctic Atmosphere, Seas and Ice Dynamics. CP, NVR and ZK acknowledge support from the ANR 469 EQUIPEX IAOOS project, through ANR-10-EQPX-32-01 grant, and the ICE-ARC programme from the European Union 7th Framework Programme, grant 603887. HK was funded through Research Council of Norway project Boom or Bust number 244646. We thank N-ICE2015 participants, the captains, crews and N-ICE2015 scientists for their help in making this study possible. We thank two anonymous reviewers for valuable comments that greatly improved the submitted manuscript. The following data sets were used in this study and are publicly available at the Norwegian Polar Data Centre: vessel-mounted CTD [Dodd et al., 2016], microstructure sonde [Meyer et al., 2016], vessel-mounted ADCP [Meyer et al., 2016], long ranger ADCP [Provost et al., 2016], and dissolved oxygen concentrations [Dodd et al., 2016] (<https://data.npolar.no/dataset/?filter-sets=N-ICE2015>). The IAOOS platform data are available at LOCEAN (Christine Provost, [cp@locean-ipsl.upmc.fr](mailto:cp@locean-ipsl.upmc.fr)).

- Dee, D. P., et al. (2011), The ERA-Interim reanalysis: Configuration and performance of the data assimilation system, *Q. J. R. Meteorol. Soc.*, 137(656), 553–597.
- Dodd, P., et al. (2016), N-ICE2015 bottle data from ship water sampler., data set, Norwegian Polar Institute, doi:10.21334/npolar.2016.516bc529.
- Dodd, P., et al. (2016), N-ICE2015 ship-based conductivity-temperature-depth (CTD) data, Data set, Norwegian Polar Institute, doi:10.21334/npolar.2017.92262a9c.
- Egbert, G. D., A. F. Bennett, and M. G. G. Foreman (1994), TOPEX/POSEIDON tides estimated using a global inverse model, *J. Geophys. Res.*, 99(C12), 24,821–24,852, doi:10.1029/94JC01894.
- Emery, W. J., and R. E. Thomson (2001), *Data Analysis Methods in Physical Oceanography*, 2nd ed., chap. 5, 638 pp., Elsevier, Amsterdam.
- Fer, I. (2006), Scaling turbulent dissipation in an Arctic fjord, *Deep Sea Res., Part II*, 53, 77–95.
- Fer, I., R. Skogseth, and F. Geyer (2010), Internal waves and mixing in the marginal ice zone near the Yermak Plateau, *J. Phys. Oceanogr.*, 40(7), 1613–1630, doi:10.1175/2010JPO4371.1.
- Fer, I., M. Müller, and A. K. Peterson (2015), Tidal forcing, energetics, and mixing near the Yermak Plateau, *Ocean Sci.*, 11, 287–304, doi:10.5194/os-11-287-2015.
- Gascard, J. C., C. Richez, and C. Rouault (1995), New insights on large-scale oceanography in Fram Strait: The West Spitsbergen Current, in *Oceanography of the Arctic: Marginal Ice Zones and Continental Shelves*, edited by W. Smith and J. Grebmeier, pp. 131–182, AGU, Washington, D. C.
- Granskog, M. A., P. Assmy, S. Gerland, G. Spreen, H. Steen, and L. H. Smedsrud (2016), Arctic research on thin ice: Understanding the consequences of ongoing Arctic sea ice loss (N-ICE2015), *Eos, Trans. AGU*, 97, 22–26, doi:10.1029/2016EO044097.
- Graham, R. M., A. Rinke, L. Cohen, S. R. Hudson, V. P. Walden, M. A. Granskog, W. Dorn, M. Kayser, and M. Maturilli (2017), A comparison of the two Arctic atmospheric winter states observed during N-ICE2015 and SHEBA, *J. Geophys. Res. Atmos.*, 122, 5716–5737, doi:10.1002/2016JD025475.
- Grotefendt, K., K. Logemann, D. Quadfasel, and S. Ronski (1998), Is the Arctic Ocean warming?, *J. Geophys. Res.*, 103(C12), 27,627–679,687.
- Hansen, E., S. Gerland, M. A. Granskog, O. Pavlova, A. H. H. Renner, J. Haapala, T. B. Løyning, and M. Tschudi (2013), Thinning of Arctic sea ice observed in Fram Strait: 1990–2011, *J. Geophys. Res. Oceans*, 118, 5202–5221, doi:10.1002/jgrc.20393.
- Hudson, S. R., L. Cohen, and V. Walden (2015), N-ICE2015 surface meteorology, Data set, Norwegian Polar Institute, doi:10.21334/npolar.2015.056a61d1.
- Ivanov, V. V., I. V. Polyakov, I. A. Dmitrenko, E. Hansen, I. A. Repina, S. S. Kirillov, C. Mauritzen, H. L. Simmons, and L. A. Timokhov (2009), Seasonal variability in Atlantic Water off Spitsbergen, *Deep Sea Res., Part I*, 56, 1–14.
- Ivanov, V. V., I. Alexeev, Vladimir Koldunov, Nikolay V. Repina, and A. Sandø, Anne Britt Smedsrud, Lars Henrik Smirnov (2016), Arctic Ocean Heat Impact on Regional Ice Decay: A Suggested Positive Feedback, *J. Phys. Oceanogr.*, 46(5), 1437–1456.
- Itkin, P., G. Spreen, B. Cheng, M. Doble, F. Girard-Arduin, J. Haapala, N. Hughes, L. Kaleschke, M. Nicolaus, and J. Wilkinson (2017), Thin ice and storms: Sea ice deformation from buoy arrays deployed during N-ICE2015, *J. Geophys. Res. Oceans*, doi:10.1002/2016JC012403, in press.
- Koenig, Z., C. Provost, N. Villaceros-Robineau, N. Sennéchaël, and A. Meyer (2016), Winter ocean-ice interactions under thin sea ice observed by IAOOS platforms during N-ICE2015: Salty surface mixed layer and active basal melt, *J. Geophys. Res. Oceans*, 121, 7898–7916, doi:10.1002/2016JC012195.
- Koenig, Z., C. Provost, N. Villaceros-Robineau, N. Sennéchaël, A. Meyer, J.-M. Lellouche, and G. Garric (2017), Atlantic waters inflow north of Svalbard: Insights from IAOOS observations and Mercator Ocean global operational system during N-ICE2015, *J. Geophys. Res. Oceans*, 122, 1254–1273, doi:10.1002/2016JC012424.
- Lindsay, R., and A. Schweiger (2015), Arctic sea ice thickness loss determined using subsurface, aircraft, and satellite observations, *Cryosphere*, 9(1), 269–283.
- Lique, C., A. M. Treguier, B. Blanke, and N. Grima (2010), On the origins of water masses exported along both sides of Greenland: A Lagrangian model analysis, *J. Geophys. Res.*, 115, C05019, doi:10.1029/2009JC005316.
- Marnela, M., B. Rudels, M. N. Houssais, A. Beszczynska-Möller, and P. B. Eriksson (2013), Recirculation in the Fram Strait and transports of water in and north of the Fram Strait derived from CTD data, *Ocean Sci.*, 9(3), 499–519, doi:10.5194/os-9-499-2013.
- McDougall, T. J., D. R. Jackett, F. J. Millero, R. Pawlowicz, and P. M. Barker (2012), A global algorithm for estimating Absolute Salinity, *Ocean Sci.*, 8(6), 1123–1134.
- Merkouriadi, I., J.-C. Gallet, G. E. Liston, C. Polashenski, R. M. Graham, A. Rösel, and S. Gerland (2017), Winter snow conditions on Arctic sea ice north of Svalbard during the Norwegian young sea ICE (N-ICE2015) expedition, *J. Geophys. Res. Atmos.*, 122, doi:10.1002/2017JD026753.
- Meyer, A., et al. (2016), N-ICE2015 ocean microstructure profiles (MSS90L), Data set, Norwegian Polar Institute, doi:10.21334/npolar.2016.774bf6ab.
- Meyer, A., I. Fer, M. Muijlwijk, L.-H. Smedsrud, J. Miguet, N. Kusse-Tiuz, and P. A. Dodd (2016), N-ICE2015 Ocean currents: Vessel Mounted acoustic Doppler current profiler, Data set, Norwegian Polar Institute, doi:10.21334/npolar.2017.e400ef79.
- Meyer, A., I. Fer, A. Sundfjord, and A. K. Peterson (2017), Mixing rates and vertical heat fluxes north of Svalbard from Arctic winter to spring, *J. Geophys. Res. Oceans*, doi:10.1002/2016JC012441, in press.
- Muench, R. D., M. G. McPhee, C. A. Paulson, and J. H. Morison (1992), Winter oceanographic conditions in the Fram Strait-Yermak Plateau region, *J. Geophys. Res.*, 97(C3), 3469–3483.
- Onarheim, I. H., L. H. Smedsrud, R. B. Ingvaldsen, and F. Nilsen (2014), Loss of sea ice during winter north of Svalbard, *Tellus, Ser. A*, 66(1), 23933.
- Padman, L., and T. M. Dillon (1991), Turbulent mixing near the Yermak Plateau during the Coordinated Eastern Arctic Experiment, *J. Geophys. Res.*, 96(C3), 4769–4782, doi:10.1029/90JC02260.
- Padman, L., and S. Y. Erofeeva (2004), A barotropic inverse tidal model for the Arctic Ocean, *Geophys. Res. Lett.*, 31, L02303, doi:10.1029/2003GL019003.
- Peralta-Ferriz, C., and R. A. Woodgate (2015), Seasonal and interannual variability of pan-Arctic surface mixed layer properties from 1979 to 2012 from hydrographic data, and the dominance of stratification for multiyear mixed layer depth shoaling, *Prog. Oceanogr.*, 134, 19–53, doi:10.1016/j.pocean.2014.12.005.
- Perkin, R. G., and E. L. Lewis (1984), Mixing in the West Spitsbergen Current, *J. Phys. Oceanogr.*, 14, 1315–1325.
- Peterson, A. K., A. Randelhoff, I. Fer, A. Meyer, L. Håvik, L. H. Smedsrud, I. Onarheim, M. Muijlwick, A. Sundfjord, and M. G. McPhee (2016), N-ICE2015 ocean turbulent fluxes from under-ice turbulent cluster (TIC), Data set, Norwegian Polar Institute, doi:10.21334/npolar.2016.ab29f1e2.
- Peterson, A. K., I. Fer, M. G. McPhee, and A. Randelhoff (2017), Turbulent heat and momentum fluxes in the upper ocean under Arctic sea ice, *J. Geophys. Res. Oceans*, 122, 1439–1456, doi:10.1002/2016JC012283.

- Polyakov, I. V., A. V. Pnyushkov, R. Rember, V. V. Ivanov, Y.-D. Lenn, L. Padman, and E. C. Carmack (2012), Mooring-based observations of double-diffusive staircases over the Laptev Sea Slope, *J. Phys. Oceanogr.*, **42**, 95–109, doi:10.1175/2011JPO4606.1.
- Polyakov, I. V., A. V. Pnyushkov, R. Rember, L. Padman, E. C. Carmack, and J. M. Jackson (2013), Winter convection transports atlantic water heat to the surface layer in the Eastern Arctic Ocean, *J. Phys. Oceanogr.*, **43**(1981), 2142–2155, doi:10.1175/JPO-D-12-0169.1.
- Prandke, H., and A. Stips (1998), Test measurements with an operational microstructure-turbulence profiler: Detection limit of dissipation rates, *Aquat. Sci.*, **60**(3), 191–209, doi:10.1007/s000270050036.
- Provost, C., et al. (2015), IAOOS (Ice-Atmosphere-Arctic Ocean Observing System, 2011–2019), *Mercator Ocean Quart. Newslett.*, **51**, 13–15.
- Provost, C., I. Onarheim, A. Randelhoff, A. Meyer, L.-H. Smedsrud, V. Rerolle, N. Villacieros Robineau, I. Fer, and A. Petersson (2016), N-ICE2015 Ocean currents: RDI Long Ranger acoustic Doppler current profiler, Data set, Norwegian Polar Institute, doi:10.21334/npolar.2017.accb9dd5.
- Randelhoff, A., A. Sundfjord, and M. Reigstad (2015), Seasonal variability and fluxes of nitrate in the surface waters over the Arctic shelf slope, *J. Geophys. Res.*, **49**, 3442–3449, doi:10.1002/2015GL063655.
- Renner, A. H. H., S. Hendricks, S. Gerland, J. Beckers, C. Haas, and T. Krumpfen (2013), Large-scale ice thickness distribution of first-year sea ice in spring and summer north of Svalbard, *Ann. Glaciol.*, **54**(62), 13–18.
- Renner, A. H. H., S. Gerland, C. Haas, G. Spreen, J. F. Beckers, E. Hansen, M. Nicolaus, and H. Goodwin (2014), Evidence of Arctic sea ice thinning from direct observations, *Geophys. Res. Lett.*, **41**, 5029–5036, doi:10.1002/2014GL060369.
- Rösel, A., et al. (2016), N-ICE2015 snow depth data with Magna Probe, Data set, Norwegian Polar Institute, doi:10.21334/npolar.2016.3d72756d.
- Rudels, B., R. Meyer, E. Fahrbach, V. V. Ivanov, S. Østerhus, D. Quadfasel, U. Schauer, V. Tverberg, and R. A. Woodgate (2000), Water mass distribution in Fram Strait and over the Yermak Plateau in summer 1997, *Ann. Geophys.*, **18**(6), 687–705, doi:10.1007/s005850000216.
- Rudels, B., E. P. Jones, U. Schauer, and P. Eriksson (2004), Atlantic sources of the Arctic Ocean surface and halocline waters, *Polar Res.*, **23**(2), 181–208.
- Rudels, B., G. Björk, J. Nilsson, P. Winsor, I. Lake, and C. Nohr (2005), The interaction between waters from the Arctic Ocean and the Nordic Seas north of Fram Strait and along the East Greenland Current: Results from the Arctic Ocean-02 Oden expedition, *J. Mar. Syst.*, **55**(1–2), 1–30.
- Rudels, B., M. Korhonen, U. Schauer, S. Pisarev, B. Rabe, and A. Wisotzki (2015), Circulation and transformation of Atlantic water in the Eurasian Basin and the contribution of the Fram Strait inflow branch to the Arctic Ocean heat budget, *Prog. Oceanogr.*, **132**, 128–152, doi:10.1016/j.pocean.2014.04.003.
- Schauer, U., H. Loeng, B. Rudels, V. K. Ozhigin, and W. Dieck (2002), Atlantic Water flow through the Barents and Kara Seas, *Deep Sea Res., Part I*, **49**(12), 2281–2298.
- Schauer, U., E. Fahrbach, S. Østerhus, and G. Rohardt (2004), Arctic warming through the Fram Strait: Oceanic heat transport from 3 years of measurements, *J. Geophys. Res.*, **109**, C06026, doi:10.1029/2003JC001823.
- Schmidtko, S., G. C. Johnson, and J. M. Lyman (2013), MIMOC: A global monthly isopycnal upper-ocean climatology with mixed layers, *J. Geophys. Res. Oceans*, **118**, 1658–1672, doi:10.1002/jgrc.20122.
- Sirevaag, A., and I. Fer (2009), Early Spring oceanic heat fluxes and mixing observed from drift stations North of Svalbard, *J. Phys. Oceanogr.*, **39**(12), 3049–3069, doi:10.1175/2009JPO4172.1.
- Spall, M. A. (2013), On the circulation of Atlantic Water in the Arctic Ocean, *J. Phys. Oceanogr.*, **43**, 2352–2371.
- Steele, M., and T. J. Boyd (1998), Retreat of the cold halocline layer in the Arctic Ocean, *J. Geophys. Res.*, **103**(C5), 10,419–10,435.
- Timmermans, M. L., R. A. Krishfield, S. Laney, and J. M. Toole (2010), Ice-Tethered profiler measurements of dissolved oxygen under permanent ice cover in the Arctic Ocean, *J. Atmos. Oceanic Technol.*, **27**(11), 1936–1949.
- Toole, J. M., M.-L. Timmermans, D. K. Perovich, R. A. Krishfield, A. Proshutinsky, and J. A. Richter-Menge (2010), Influences of the ocean surface mixed layer and thermohaline stratification on Arctic Sea ice in the central Canada Basin, *J. Geophys. Res.*, **115**, C10,018, doi:10.1029/2009JC005660.
- Treshnikov, A. F. (1977), Polar oceans, in *Polar Oceans*, edited by M. Dunbar, pp. 17–31, Arctic Inst. North Am., Calgary, Alberta, Canada.
- Untersteiner, N. (1988), On the ice and heat balance in Fram Strait, *J. Geophys. Res.*, **93**(7), 527–531.
- Våge, K., R. S. Pickart, V. Pavlov, P. Lin, D. J. Torres, R. B. Ingvaldsen, A. Sundfjord, and A. Proshutinsky (2016), The Atlantic Water boundary current in the Nansen Basin: Transport and mechanisms of lateral exchange, *J. Geophys. Res. Oceans*, **121**, 6946–6960, doi:10.1002/2016JC011715.
- Weiss, R. F. (1970), The solubility of nitrogen, oxygen and argon in water and seawater, *Deep Sea Res. Oceanogr. Abstr.*, **17**(4), 721–735.
- Wijesekera, H. W., L. Padman, T. M. Dillon, M. Levine, C. Paulson, and R. Pinkel (1993), The application of internal-wave dissipation models to a region of strong mixing, *J. Phys. Oceanogr.*, **23**(2), 269–286.
- Willmes, S., and G. Heinemann (2016), Sea-ice wintertime lead frequencies and regional characteristics in the Arctic, 2003–2015, *Remote Sens.*, **8**(1).

## Erratum

In the originally published version of this article, the reference for *Graham et al.* [2017] was incomplete. This has since been updated and this version may be considered the authoritative version of record.